The Astrophysical Journal Letters, 951:L22 (19pp), 2023 July 1 https://doi.org/10.3847/2041-8213/acdd54

Spectroscopic Confirmation of CEERS NIRCam-selected Galaxies at $z \simeq 8$–10

Pablo Arrabal Haro[1], Mark Dickinson[1], Steven L. Finkelstein[2], Seiji Fujimoto[2,37], Vital Fernández[3], Jeyhan S. Kartaltepe[4], Intae Jung[5], Justin W. Cole[6,7], Denis Burgarella[8], Katherine Chworowsky[2,38], Taylor A. Hutchison[9,39], Alexa M. Morales[2], Casey Papovich[6,7], Raymond C. Simons[10], Ricardo O. Amorín[3,11], Bren E. Backhaus[10], Micaela B. Bagley[2], Laura Bisigello[12,13], Antonello Calabrò[14], Marco Castellano[14], Nikko J. Cleri[6,7], Romeel Davé[15,16], Avishai Dekel[17], Henry C. Ferguson[5], Adriano Fontana[14], Eric Gawiser[18], Mauro Giavalisco[19], Santosh Harish[4], Nimish P. Hathi[5], Michaela Hirschmann[20], Benne W. Holwerda[21], Marc Huertas-Company[22,23,24], Anton M. Koekemoer[5], Rebecca L. Larson[2,38], Ray A. Lucas[5], Bahram Mobasher[25], Pablo G. Pérez-González[26], Nor Pirzkal[27], Caitlin Rose[4], Paola Santini[14], Jonathan R. Trump[10], Alexander de la Vega[25], Xin Wang[28,29,30], Benjamin J. Weiner[31], Stephen M. Wilkins[32,33], Guang Yang[34,35], L. Y. Aaron Yung[9,39], and Jorge A. Zavala[36]

[1] NSF's National Optical-Infrared Astronomy Research Laboratory, 950 N. Cherry Ave., Tucson, AZ 85719, USA; parrabalh@gmail.com
[2] Department of Astronomy, The University of Texas at Austin, Austin, TX, USA
[3] Instituto de Investigación Multidisciplinar en Ciencia y Tecnología, Universidad de La Serena, Raul Bitrán 1305, La Serena 2204000, Chile
[4] Laboratory for Multiwavelength Astrophysics, School of Physics and Astronomy, Rochester Institute of Technology, 84 Lomb Memorial Drive, Rochester, NY 14623, USA
[5] Space Telescope Science Institute, 3700 San Martin Dr., Baltimore, MD 21218, USA
[6] Department of Physics and Astronomy, Texas A&M University, College Station, TX 77843-4242 USA
[7] George P. and Cynthia Woods Mitchell Institute for Fundamental Physics and Astronomy, Texas A&M University, College Station, TX 77843-4242 USA
[8] Aix Marseille Univ, CNRS, CNES, LAM Marseille, France
[9] Astrophysics Science Division, NASA Goddard Space Flight Center, 8800 Greenbelt Rd, Greenbelt, MD 20771, USA
[10] Department of Physics, 196 Auditorium Road, Unit 3046, University of Connecticut, Storrs, CT 06269, USA
[11] Departamento de Astronomía, Universidad de La Serena, Av. Juan Cisternas 1200 Norte, La Serena 1720236, Chile
[12] Dipartimento di Fisica e Astronomia "G.Galilei", Universitá di Padova, Via Marzolo 8, I-35131 Padova, Italy
[13] INAF–Osservatorio Astronomico di Padova, Vicolo dell'Osservatorio 5, I-35122 Padova, Italy
[14] INAF—Osservatorio Astronomico di Roma, via di Frascati 33, 00078 Monte Porzio Catone, Italy
[15] Institute for Astronomy, University of Edinburgh, Blackford Hill, Edinburgh EH9 3HJ UK
[16] Department of Physics and Astronomy, University of the Western Cape, Robert Sobukwe Rd, Bellville, Cape Town 7535, South Africa
[17] Racah Institute of Physics, The Hebrew University of Jerusalem, Jerusalem 91904, Israel
[18] Department of Physics and Astronomy, Rutgers, the State University of New Jersey, Piscataway, NJ 08854, USA
[19] University of Massachusetts Amherst, 710 North Pleasant Street, Amherst, MA 01003-9305, USA
[20] Institute of Physics, Laboratory of Galaxy Evolution, Ecole Polytechnique Fédérale de Lausanne (EPFL), Observatoire de Sauverny, 1290 Versoix, Switzerland
[21] Physics & Astronomy Department, University of Louisville, Louisville, KY 40292, USA
[22] Instituto de Astrofísica de Canarias, La Laguna, Tenerife, Spain
[23] Universidad de la Laguna, La Laguna, Tenerife, Spain
[24] Université Paris-Cité, LERMA—Observatoire de Paris, PSL, Paris, France
[25] Department of Physics and Astronomy, University of California, 900 University Ave, Riverside, CA 92521, USA
[26] Centro de Astrobiología (CAB), CSIC-INTA, Ctra. de Ajalvir km 4, Torrejón de Ardoz, E-28850 Madrid, Spain
[27] ESA/AURA Space Telescope Science Institute, USA
[28] School of Astronomy and Space Science, University of Chinese Academy of Sciences (UCAS), Beijing 100049, People's Republic of China
[29] National Astronomical Observatories, Chinese Academy of Sciences, Beijing 100101, People's Republic of China
[30] Institute for Frontiers in Astronomy and Astrophysics, Beijing Normal University, Beijing 102206, People's Republic of China
[31] MMT/Steward Observatory, University of Arizona, 933 N. Cherry Ave., Tucson, AZ 85721, USA
[32] Astronomy Centre, University of Sussex, Falmer, Brighton BN1 9QH, UK
[33] Institute of Space Sciences and Astronomy, University of Malta, Msida MSD 2080, Malta
[34] Kapteyn Astronomical Institute, University of Groningen, P.O. Box 800, 9700 AV Groningen, The Netherlands
[35] SRON Netherlands Institute for Space Research, Postbus 800, 9700 AV Groningen, The Netherlands
[36] National Astronomical Observatory of Japan, 2-21-1 Osawa, Mitaka, Tokyo 181-8588, Japan
Received 2023 April 11; revised 2023 June 6; accepted 2023 June 8; published 2023 July 6

Abstract

We present JWST/NIRSpec prism spectroscopy of seven galaxies selected from Cosmic Evolution Early Release Science (CEERS) survey NIRCam imaging with photometric redshifts $z_{\rm phot} > 8$. We measure emission line redshifts of $z = 7.65$ and 8.64 for two galaxies. For two other sources without securely detected emission lines we measure $z = 9.77^{+0.37}_{-0.29}$ and $10.01^{+0.14}_{-0.19}$ by fitting model spectral templates to the prism data, from which we detect continuum breaks consistent with Lyα opacity from a mostly neutral intergalactic medium. The presence of strong

[37] Hubble Fellow.
[38] NSF Graduate Fellow.
[39] NASA Postdoctoral Fellow.

breaks and the absence of strong emission lines give high confidence that these two galaxies have redshifts $z > 9.6$, but the redshift values derived from the breaks alone have large uncertainties given the low spectral resolution and relatively low S/N of the CEERS NIRSpec prism data. The two $z \sim 10$ sources observed are relatively luminous ($M_{\rm UV} < -20$), with blue continua ($-2.3 \lesssim \beta \lesssim -1.9$) and low dust attenuation ($A_V \simeq 0.15^{+0.3}_{-0.1}$); and at least one of them has a high stellar mass for a galaxy at that redshift ($\log(M_\star/M_\odot) \simeq 9.3^{+0.2}_{-0.3}$). Considered together with spectroscopic observations of other CEERS NIRCam-selected high-z galaxy candidates in the literature, we find a high rate of redshift confirmation and low rate of confirmed interlopers (8%). Ten out of 35 $z > 8$ candidates with CEERS NIRSpec spectroscopy do not have secure redshifts, but the absence of emission lines in their spectra is consistent with redshifts $z > 9.6$. We find that $z > 8$ photometric redshifts are generally in agreement (within their uncertainties) with the spectroscopic values, but also that the photometric redshifts tend to be slightly overestimated ($\langle \Delta z \rangle = 0.45 \pm 0.11$), suggesting that current templates do not fully describe the spectra of very-high-z sources. Overall, the spectroscopy solidifies photometric redshift evidence for a high spatial density of bright galaxies at $z > 8$ compared to theoretical model predictions, and further disfavors an accelerated decline in the integrated UV luminosity density at $z > 8$.

Unified Astronomy Thesaurus concepts: Early universe (435); Galaxy evolution (594); Galaxy formation (595); High-redshift galaxies (734)

1. Introduction

Understanding galaxy formation and evolution during the first hundreds of megayears in the history of the universe has been and remains one of the biggest astronomical challenges of the last decades. Extensive studies based on deep observations with the Hubble Space Telescope (HST), the Spitzer Space Telescope, and the largest ground-based facilities have set constraints on the abundance and physical properties of such early galaxies at redshifts below $z \lesssim 9$ (e.g., Ellis et al. 2013; McLure et al. 2013; Matthee et al. 2014; Bouwens et al. 2015; Finkelstein et al. 2015; Oesch et al. 2018; Sobral et al. 2018; Stefanon et al. 2019; Bowler et al. 2020; Finkelstein & Bagley 2022, among others).

The advent of JWST is quickly revolutionizing the exploration of the early universe within its first ∼200–600 Myr. Several works have built up samples of galaxy candidates at $z \sim 8$–17 in the first deep JWST/NIRCam (Rieke et al. 2003, 2005; Beichman et al. 2012) imaging available from the Early Release Observations (ERO), Early Release Science (ERS), and treasury programs (Castellano et al. 2022; Finkelstein et al. 2022; Naidu et al. 2022b; Adams et al. 2023; Atek et al. 2023; Austin et al. 2023; Bouwens et al. 2023; Donnan et al. 2023; Finkelstein et al. 2023; Harikane et al. 2023b; Rodighiero et al. 2023; Yan et al. 2023). Apart from the initial public data, studies from Guaranteed Time Observations (GTO) projects have also presented other very-high-z samples, making use of deeper imaging data (Pérez-González et al. 2023b; Robertson et al. 2023; Tacchella et al. 2023).

The abundance and brightness of early galaxies found in these studies seem to be in tension with the predictions from most cosmological models (e.g., Boylan-Kolchin 2023; Ferrara et al. 2023; Finkelstein et al. 2023; Mason et al. 2023; Pérez-González et al. 2023b). However, it is important to keep in mind the caveats associated with broadband-selected high-z samples (see, e.g., Arrabal Haro et al. 2018), especially when working with a complex, brand new observing facility such as JWST to study the still quite unexplored $z \gtrsim 8$ redshift regime. Zavala et al. (2023), for instance, showed that dust-enshrouded galaxies at lower redshifts ($z \lesssim 7$) could be misidentified as very-high-z objects. This can occur when a combination of a strong Balmer break with high dust attenuation and strong nebular emission lines result in spectral energy distributions (SEDs) that resemble the emission-dropout signature employed for the selection of Lyman-break galaxies (LBGs) at high redshift (see, e.g., Giavalisco 2002). Indeed, this possibility has been verified by recent observations using JWST/NIRSpec (Jakobsen et al. 2022) to study promising $z > 10$ candidates from the Cosmic Evolution Early Release Science (CEERS) survey (S. L. Finkelstein et al. 2023, in preparation). One galaxy with a persuasive photometric redshift $z \approx 16$ was instead shown to have $z = 4.9$, with strong line emission affecting flux measurements in several NIRSpec photometric bands and mimicking the SED of a galaxy at much higher redshift (Arrabal Haro et al. 2023). Moreover, Bouwens et al. (2023) reported discrepancies in high-z samples assembled by independent works from the same public data sets, highlighting the differences in the selection criteria employed and the need for more refined JWST instrumental calibrations.

Spectroscopic confirmation of such early galaxies is therefore crucial to validate our current photometric samples, identify possible sources of interlopers in the new $z \gtrsim 8$ regime we are starting to explore in detail beyond HST's observational boundaries, and help in refining our high-z selection criteria. Only after spectroscopic follow up of a statistically significant fraction of the current $z \gtrsim 8$ candidates, will we get a good idea of the reliability of the very-high-z photometric samples. That will in turn result in a better characterization of the number density of these early galaxies in the heart of the Epoch of Reionization (EoR).

Among the spectroscopic observations of $z > 8$ sources carried out so far, Williams et al. (2023) reported a low-mass highly magnified $z = 9.51$ galaxy in Director's Discretionary (DD) NIRSpec observations of the galaxy cluster RX J2129. On the other hand, Boyett et al. (2023) presented a low-magnification massive $z = 9.31$ source with high-resolution NIRSpec observations around the A2744 galaxy cluster from the GLASS-JWST-ERS program (Treu et al. 2022). Several $z \gtrsim 8$ candidates from CEERS have been also observed with NIRSpec (Fujimoto et al. 2023; Heintz et al. 2023; Tang et al. 2023) with promising confirmation rates.

Confirmation of galaxies with redshifts $z \gtrsim 9.6$ becomes more challenging as strong emission lines like Hβ and [O III] 4960, 5008 Å redshift beyond the long wavelength limit of NIRSpec (∼5.3 μm for the NIRSpec prism). For the relatively high nebular excitation conditions that are typically observed for galaxies at these redshifts (e.g., Matthee et al. 2023; Tang et al. 2023; Trump et al. 2023), emission lines at wavelengths bluer than Hβ are usually faint and Lyα emission is often strongly attenuated by the highly neutral intergalactic medium

(IGM; Dijkstra 2014; Hayes 2015). However, the low spectral resolution of the NIRSpec prism offers excellent sensitivity for detecting the redshifted ultraviolet continuum emission from galaxies at the EoR, and hence the strong break at Lyα due to the opacity of the IGM.

To date, only a few galaxies have been spectroscopically confirmed with NIRSpec at $z > 9.6$. Roberts-Borsani et al. (2023) confirmed a highly magnified $z = 9.76$ galaxy lensed by the A2744 galaxy cluster, and a $z = 10.17$ galaxy triply lensed by the MACSJ0647.7+7015 galaxy cluster was also reported in Harikane et al. (2023a) and Hsiao et al. (2023). Three galaxies at $z = 10.1$, 11.0, and 11.4 have been confirmed by DD observations of the CEERS field (Arrabal Haro et al. 2023; Harikane et al. 2023a). Finally, the JWST Advanced Deep Extragalactic Survey (JADES) GTO project has presented five others: Bunker et al. (2023) measured an unambiguous redshift of 10.60 for GN-z11, slightly below previous estimates (Oesch et al. 2016; Jiang et al. 2021), while Curtis-Lake et al. (2023) presented four other galaxies at $z > 10$, including the most distant spectroscopic confirmation at $z = 13.2$, identified in deep GTO NIRCam observations (Robertson et al. 2023).

Here we present the spectroscopic confirmation of four $z > 8$ galaxies in late CEERS NIRSpec prism observations, including two galaxies at $z \approx 9.75$–10. This work is structured as follows: Section 2 describes the NIRCam data used to select our targets as well as the NIRSpec observations and data reduction. Section 3 shows the redshift measurements and SED fitting of the galaxies; the main results are discussed in Section 4 and summarized in Section 5. All magnitudes are in the AB system (Oke & Gunn 1983) and all uncertainty intervals correspond to the 16–84th percentiles of the values. Throughout this work we use a Planck Collaboration et al. (2020) flat Λ cold dark matter (ΛCDM) cosmology with $H_0 = 67.36$ km s^{-1} Mpc^{-1} and $\Omega_m = 0.315$.

2. Observations and Data Reduction

2.1. NIRCam Data and Sample Definition

We selected candidate spectroscopic targets from the CEERS NIRCam imaging data in the CANDELS (Grogin et al. 2011; Koekemoer et al. 2011) EGS field. Here we use the full set of 10 CEERS NIRCam pointings, including data obtained in CEERS epoch 2 (2022 December), which were reduced in the same way as the epoch 1 (2022 June) pointings as described in detail in Bagley et al. (2023). Photometry was performed on these mosaics in a similar manner as described in Finkelstein et al. (2023), with a few key differences regarding point-spread function (PSF) matching. To derive accurate total fluxes, all bands with PSFs smaller than that of F277W (i.e., Advanced Camera for Surveys (ACS) F606W and F814W, and NIRCam F115W, F150W, and F200W) had their images convolved to match the F277W PSF. For images with larger PSFs than F277W (i.e., NIRCam F356W, F410M, and F444W, and WFC3 F105W, F125W, F140W, and F160W), fluxes were measured in the native images, but a correction was applied. This correction was derived on a per-source basis as the ratio of the flux in the native F277W image to that of the F277W image convolved to match the PSF in a given image. In this manner, we derive accurate colors without blurring all images to match F444W (as was done by Finkelstein et al. 2023), with the underlying assumption that there are no significant morphological K-corrections from observed ~1–3 or 3–5 μm. Finally, accurate total fluxes were estimated via source-injection simulations, here deriving a magnitude-dependent correction factor (from ~a few percent for bright galaxies, to ~10% for faint galaxies).

Photometric redshifts were derived using EAZY (Brammer et al. 2008), employing the default set of 12 Flexible Stellar Population Synthesis (FSPS) templates, along with the additional blue templates designed by Larson et al. (2022) for the $z > 8$ universe. Candidate $z > 8$ galaxies were selected in an identical manner as in Finkelstein et al. (2023), thus we refer the reader there for more details.

2.2. MIRI Imaging Data

One of the galaxies in the sample (CEERS_35590/MSA ID 80041) falls in the area covered by the CEERS JWST/MIRI imaging for field 9, acquired in CEERS epoch 2 (2022 December). MIRI photometry in the F560W and F770W bands extend the SED measurement to longer wavelengths than those observed by NIRCam and NIRSpec. The data were processed following the procedures discussed elsewhere (Papovich et al. 2023; Yang et al. 2023). This produced final science, rms, and weight-map images registered astrometrically to the NIRCam imaging. The rms image includes estimates for the Poisson noise, readout noise, and correlated pixel noise (see Yang et al. 2023).

We measured photometry in the MIRI imaging following the steps in Papovich et al. (2023). We first matched the image quality of the F560W image to the F770W image and constructed a weighted-sum "detection image" of the two. We then measured source photometry using `Source Extractor` (version 2.19.5, Bertin & Arnouts 1996) in "dual-image" mode using the detection image and its weight map for object detection and measuring object fluxes and uncertainties in the F560W and F770W images using the parameters in Papovich et al. (2023), and scaling to a total magnitude using the `MAG_AUTO` aperture derived from the F560W+F770W detection image.

Formally, CEERS_35590 is detected, albeit weakly, with measured flux values of f_ν(F560W) $= 47 \pm 28$ nJy and f_ν(F770W) $= 84 \pm 29$ nJy. We include these measurements in the analysis of the galaxy SED below (see Section 3.3).

2.3. NIRSpec Observations and MSA Target Selection

The NIRSpec Micro Shutter Array (MSA; Ferruit et al. 2022) data here presented come from the rescheduling of two of the original CEERS pointings whose prism observations were affected by an electrical short in CEERS epoch 2 (2022 December). The rescheduled prism observations were executed in 2023 February, enabling the selection of new high-z candidates from the CEERS epoch 2 NIRCam images, as described in Section 2.1. High-redshift candidates from the 2022 December CEERS NIRSpec observations are presented in Fujimoto et al. (2023).

The CEERS epoch 3 NIRSpec pointings (NIRSpec11 and NIRSpec12) followed the same observing configuration as previous CEERS MSA observations, namely, three integrations of 14 groups in NRSIRS2 readout mode per visit, for a total exposure time of 3107 s. Three-shutter slitlets were used, enabling a three-point nodding pattern to facilitate background subtraction. The disperser employed was the prism, which covers the wavelength range 0.6–5.3 μm with varying spectral

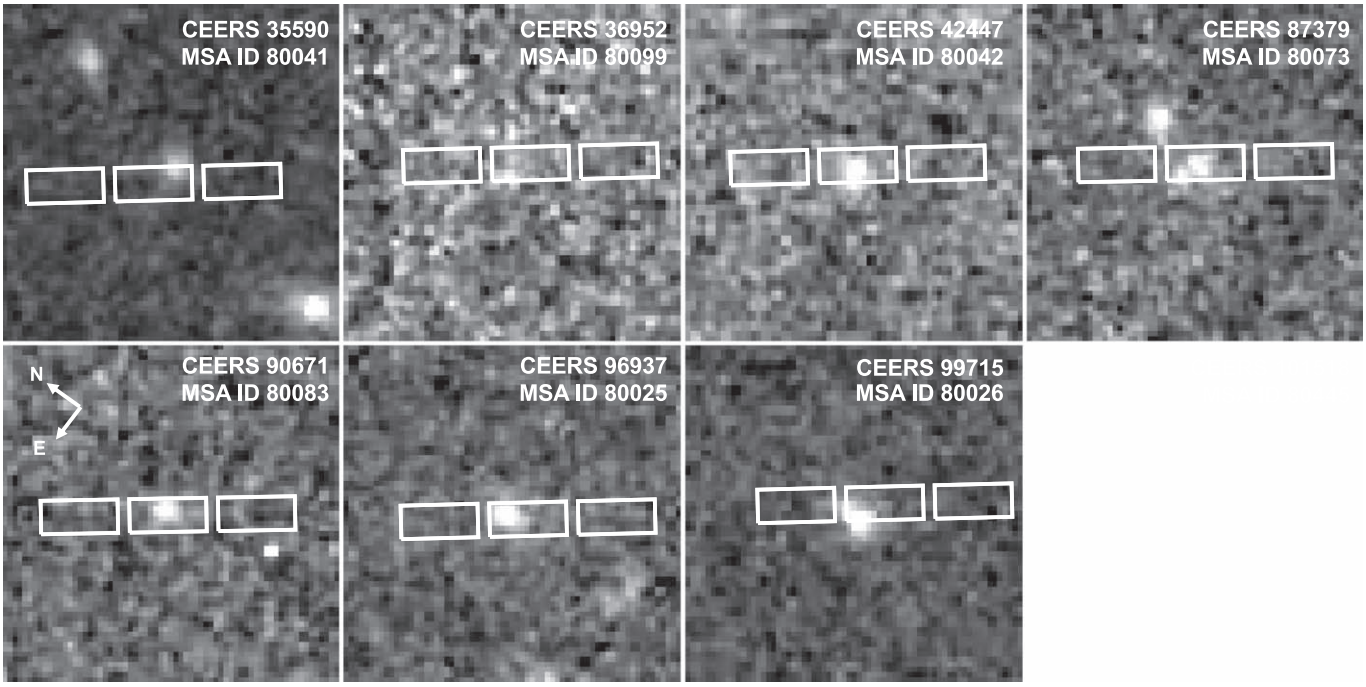

Figure 1. F277W $2'' \times 2''$cutouts of the seven NIRCam-selected $z > 8$ candidates included in CEERS epoch 3 NIRSpec MSA observations with the NIRSpec MSA shutter positions overlaid.

resolution $R \equiv \lambda/\Delta\lambda \approx 30$ at $\lambda = 1.2\,\mu$m to >300 at $\lambda > 5\,\mu$ m. The low resolution of the prism at bluer wavelengths aids the detection of any faint UV continuum and the Lyα break, while the higher resolution at red wavelengths facilitates the detection of redshifted rest-frame optical emission lines.

In addition, the observing configuration in NIRSpec11 was observed twice, introducing a shift of ~67 mas (1/3 of a shutter width) along the dispersion direction in the second visit. This was done to provide a way to test slit losses as a function of source centering within the NIRSpec microshutters. The locations of the two new prism pointings were selected to maximize the yield of NIRCam-selected $z \gtrsim 8$ candidates. In order to support the slit loss test, the NIRSpec11 pointing was also constrained to ensure overlap with CEERS NIRCam grism slitless spectroscopic observations.

The final MSA configurations included a total of seven NIRCam-selected $z > 8$ galaxy candidates. Image cutouts of these candidates are shown in Figure 1.

2.4. NIRSpec Data Reduction

The NIRSpec data processing will be explained in detail in P. Arrabal Haro et al. (2023, in preparation). The main steps of the reduction follow those employed in Fujimoto et al. (2023), Kocevski et al. (2023), and Larson et al. (2023), as summarized below.

We make use of the STScI Calibration Pipeline[40] version 1.8.5 and the Calibration Reference Data System (CRDS) mapping 1061, with the pipeline modules separated into three stages.

In stage one (using the `calwebb_detector1` pipeline module), we correct for detector $1/f$ noise, subtract the dark current and bias, and generate count-rate maps (CRMs) from the uncalibrated images. We modified the parameters of the `jump` step to gain an improved correction of the "snowball" events[41] often seen in the raw data (associated with high-energy cosmic rays).

The resulting CRMs are then processed through stage two using the `calwebb_spec2` pipeline module. At this stage, the pipeline creates two-dimensional (2D) cutouts of the slitlets (each made up of three shutters), corrects flat-fielding, runs background subtraction making use of the three-nod pattern, executes the photometric and wavelength calibrations, and resamples the 2D spectra to correct distortions of the spectral trace. We adopt the default pipeline slit loss correction implemented in the `pathloss` step.

In the final stage (using the `calwebb_spec3` pipeline module), we combine the images of the three nods, using customized apertures in extracting the one-dimensional (1D) spectra. The custom extraction apertures are determined by visually identifying high signal-to-noise ratio (S/N) continuum or emission lines in our targets, features which are easily recognizable in the 2D spectra. In the case where a source is too faint for any robust visual identification, we define a 4 pixel extraction aperture around a central spatial location estimated from the relative position of the target within its shutter, which we derive from the MSA configuration. Lastly, the 2D and 1D spectra are simultaneously inspected using the Mosviz visualization tool[42] (Developers et al. 2023) in order to mask any possible remaining hot pixels or other artifacts within the images, as well as the detector gap (when present).

The JWST pipeline uses an instrumental noise model to calculate flux errors for the extracted spectra. As described in Appendix B, we test these flux errors and rescale them for the effect of interpolation introduced by the pipeline when resampling the data.

[40] https://jwst-pipeline.readthedocs.io/en/latest/index.html

[41] https://jwst-docs.stsci.edu/data-artifacts-and-features/snowballs-and-shower-artifacts

[42] https://jdaviz.readthedocs.io/en/latest/mosviz/index.html

3. Analysis

3.1. Redshift Measurement

We measure redshifts from the spectra via several methods. A first estimation is performed for the sources with emission lines by Gaussian fitting of the [O III] 5008 Å line. The line fittings and redshift calculation are performed using LIME[43] (see Fernández et al. 2023) on the observed frame.

Second, we try three separate methods to measure the redshift via the Lyα break:

1. MCMC1: for the first method, we first create a simplified model spectrum which has three free parameters that describe a sharp Lyα break with a power-law spectral slope redward of the break. These parameters are the redshift, the UV absolute magnitude at 1500 Å ($M_{\rm UV}$), and the UV spectral slope (β). We note that this model intrinsically assumes the break is sharp. We then include the effect of Lyα damping wing absorption by adding two additional parameters: the neutral hydrogen fraction ($x_{\rm HI}$) and an ionized bubble radius ($R_{\rm bubble}$). This latter component was introduced by Curtis-Lake et al. (2023) to account for the Lyα damping wing and therefore derive more accurate continuum-break-based redshifts in the EoR.

   We derive posterior constraints on these five parameters using an IDL implementation of the EMCEE (Foreman-Mackey et al. 2013) Python code (see Finkelstein et al. 2019 for details). This procedure maximizes the likelihood that the model described by these five free parameters matches the observed prism spectrum for a given source. For each step in the Markov Chain Monte Carlo (MCMC) algorithm, the intrinsic spectrum is first generated via the draw of z, $M_{\rm UV}$, and β. Then Lyα damping wing absorption is applied following Equation (30) from Dijkstra (2014), where the damping wing optical depth is primarily dependent on photon frequency, characterized by the velocity offset. This velocity offset is computed at each wavelength as being proportional to the rest-frame difference between that wavelength and Lyα. The model spectrum is then smoothed by two pixels to match the approximate resolution of the prism data. A likelihood is then calculated assuming the uncertainties are Gaussian, and restricting the spectrum to wavelengths below rest-frame 2500 Å for a given redshift (and omitting regions where emission lines are expected). Results are derived from the posterior distributions of these five parameters from a chain consisting of 10^5 steps following a 10^6 step burn-in process.
2. MCMC2: similarly, the Lyα break redshifts are also calculated using another version of the redshift estimator that is based on the same methodology described for method (1) but uses a separate MCMC sampler package from Jung et al. (2017). We derive the posterior distributions of the five parameters similarly to method (1). We have flat priors for all parameters, and the log-likelihood is $-\chi^2/2$ between the modeled transmitted spectrum and observed spectrum. An additional 5% of systemic errors are applied in the χ^2 estimation. We employ the Metropolis-Hastings algorithm (Metropolis et al. 1953; Hastings 1970) in the MCMC sampling. The MCMC sampler checks for sampling convergence in a 10^4 step burn-in process, and the posterior distributions of the parameters are constructed from 10^4 chain steps. The fitting results take the median values of the posterior with 1σ uncertainties from central 68% confidence ranges in the posterior.
3. "Modified EAZY": we perform a third estimation of the Lyα break redshift using the SED fitting code EAZY. In this approach, we create a top-hat filter response at each wavelength of the prism spectrum and treat the spectrum as a set of pseudo-narrow-band photometry. We adopt a 2 pixel wavelength range as the filter response width for the top-hat filter response. We then use the convolved 2 pixel photometry and filter files to run EAZY on the region of the spectrum around the Lyα break ($\lambda_{\rm obs} < 2.5$ μm, hereafter "EAZY-break"). To recover the color space of blue, young galaxies, we utilize the six templates from Larson et al. (2022) in addition to the default 12 FSPS templates. An additional redshift estimation ("EAZY-full") is carried out by applying this same methodology over the complete spectrum, instead of being limited to the wavelengths around the Lyα break.

   It is important to note that with this methodology, no assumptions about the nature of the dropout are made; low-z solutions are considered equally, whereas, for the two methods described above, the assumption of a Lyα break limits the estimations to high-z solutions.

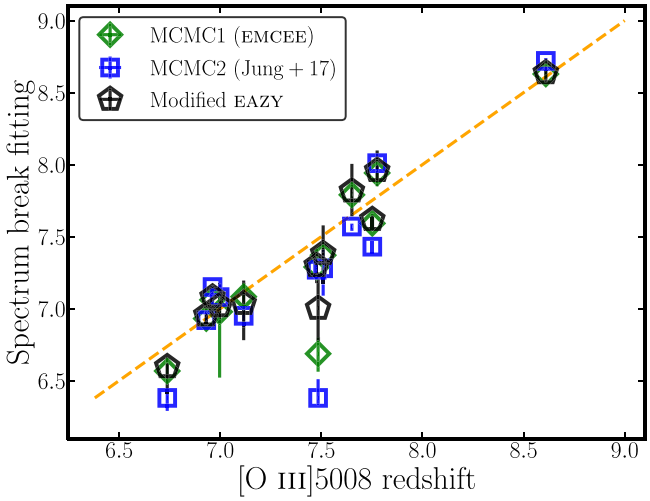

Figure 2. Lyα break redshift estimations for CEERS sources at $z > 6.6$ with detections of both the Lyα break and emission lines in NIRSpec prism spectra. Several different break redshift measurements are compared to the redshifts derived from the [O III] 5008 Å line, here taken as the fiducial redshifts of the objects. Three methods are used to fit the Lyα break, as described in the text: MCMC1 (EMCEE), MCMC2 (Jung et al. 2017), and modified EAZY. These are represented by the blue squares, green diamonds, and black pentagons, respectively. The one-to-one relation is shown as a dashed orange line.

In order to calibrate the accuracy of the Lyα break redshifts, we apply our three Lyα break fitting algorithms described above to a subsample of 12 galaxies at $6.6 < z < 8.7$ with good detections of both the Lyα break and emission lines in CEERS NIRSpec prism spectroscopy. We compare the resulting Lyα break redshifts with the [O III] 5008 Å redshifts in Figure 2. The performances of the three methodologies are similar, reporting good redshift estimations ($|\Delta z|/(1+z_{\rm [OIII]}) < 0.05$) for all sources except one (CEERS_85358, MSA ID 80372;

[43] https://lime-stable.readthedocs.io/en/latest/

Table 1
Redshift Measurements of the CEERS Epoch 3 NIRCam-selected Candidates at $z > 8$

MSA ID	R.A. (deg)	Decl. (deg)	$z_{\rm phot}$	$z_{\rm spec}^{\rm [OIII]}$	$z_{\rm spec}^{\rm break,MCMC1}$	$z_{\rm spec}^{\rm break,MCMC2}$	$z_{\rm spec}^{\rm break,EAZY}$	$z_{\rm spec}^{\rm EAZY}$
(1)	(2)	(3)	(4)	(5)	(6)	(7)	(8)	(9)
80041	214.732525	52.758090	$10.15^{+0.36}_{-0.42}$	—	$8.71^{+0.18}_{-0.05}$	$8.40^{+0.79}_{-0.22}$	$9.15^{+0.83}_{-0.91}$	$10.01^{+0.14}_{-0.19}$
80026	214.811852	52.737110	$9.76^{+0.60}_{-0.09}$	—	$9.63^{+0.20}_{-0.15}$	$9.74^{+0.33}_{-0.33}$	$9.77^{+0.37}_{-0.29}$	$10.01^{+0.18}_{-0.30}$
80083	214.961276	52.842364	$8.68^{+0.21}_{-0.27}$	$8.638^{+0.001}_{-0.001}$	—	—	—	$8.64^{+0.01}_{-0.02}$
80025	214.806065	52.750867	$8.47^{+0.15}_{-0.24}$	$7.651^{+0.001}_{-0.001}$	$7.79^{+0.07}_{-0.07}$	$7.57^{+0.02}_{-0.03}$	$7.82^{+0.19}_{-0.18}$	$7.63^{+0.02}_{-0.01}$

Note. (1) Source ID in the CEERS MSA observations. (2) R.A.(J2000). (3) Decl.(J2000). (4) Photometric redshift measured as in Finkelstein et al. (2023). (5) Spectroscopic redshift derived from [O III] 5008 Å. (6)–(8) Spectroscopic redshift derived from the fit of the Lyα break through the three methods described in Section 3.1. (9) Spectroscopic redshift derived from the EAZY-based methodology applied to the full wavelength coverage of the spectra.

$z_{\rm [OIII]} = 7.48$) with faint Lyα emission, whose redshift is more accurately determined by the EAZY-based approach. The global rms scatter of Δz is 0.18, 0.26, and 0.38 for the EAZY-based ("modified EAZY"), the EMCEE MCMC-based (MCMC1), and the Jung et al. (2017) MCMC-based (MCMC2) methods, respectively. When omitting the single source with the largest deviation, rms(Δz) goes down to 0.12, 0.12, and 0.21 for the same three methods, with an average $\langle \Delta z \equiv z_{\rm break} - z_{\rm [OIII]} \rangle$ of -0.05, -0.09, and -0.16, respectively. Based on this test, we adopt the redshift value from the EAZY-based Lyα break fitting when the estimations from the different Lyα break methodologies are consistent. For reference, we measure rms(Δz) = 0.76 when comparing the photometric redshifts against the [O III]-derived value for the galaxies employed in this test.

Four out of the seven NIRCam-selected $z > 8$ candidates have their continuum and/or emission lines detected with high enough S/N to measure redshifts (see Table 1). The 2D and 1D spectra of these four sources are presented in Figure 3. Two galaxies have emission lines from the [O III] doublet and (clear or tentative) Hβ at $7.65 \leqslant z \leqslant 8.64$. The Ly$\alpha$ continuum break is also detected for one of these galaxies. Two other galaxies show continuum breaks near 1.3 μm without clearly identifiable emission lines. We discuss these two galaxies in greater detail in the following subsection.

3.1.1. CEERS_99715 and CEERS_35590

The spectra for galaxies CEERS_99715 (MSA ID 80026) and CEERS_35590 (MSA ID 80041) exhibit breaks at $\lambda \approx 1.3$ μm, with little to no flux detected at shorter wavelengths. Integrating the spectra over the wavelength intervals 1.35–1.75 μm and 0.85–1.25 μm, above and below the breaks, yields S/N = 11.8 and 0.0 for CEERS_99715 and 12.1 and 1.0 for CEERS_35590, respectively. By eye, the break for CEERS_99715 appears to be "sharper", while that for CEERS_35590 seems more gradual, but given the low S/N per pixel (<3 at $\lambda < 1.4$ μm) this apparent difference may not be significant.

For CEERS_99715, the 2D and 1D spectra show what appears to be an emission line that peaks at the reddest pixel in the spectral range (5.294 μm), as if the line were truncated by the bandpass cutoff and/or the pipeline processing. In the rectified 2D spectrum the putative line is centered in the cross-dispersion direction within 0.5 pixels of the blue continuum, and visual inspection of the three separate nods shows that it appears to be detected in each. Although the line seems highly significant by eye, the FLUX_ERROR in the last pixel of the 1D extraction is several orders of magnitude larger than that in the adjacent (bluer) pixel. The elevated error value may be an artifact of the pipeline processing, but it suggests caution interpreting features at the very extremes of the spectral range.

If the apparent emission line in CEERS_99715 were [O III] 5008 Å, [O III] 4960 Å, or Hβ, the corresponding redshifts would be $z = 9.570$, 9.672, or 9.886, respectively. Given the low spectral resolution of the NIRSpec prism at blue wavelengths, any of these redshifts would be roughly consistent (within 2 pixels) with a Lyα break at $\sim$1.3 μm. However, in each case we would expect to detect other emission lines in the spectrum (see Figure 4). If the putative line were [O III] 5008 Å we would expect [O III] 4960 Å at one third the strength (Storey & Zeippen 2000), and perhaps also Hβ and other Balmer lines. For [O III] 4960 Å we may also expect Hβ, and if the line were Hβ we should detect Hγ unless there is significant nebular reddening, which seems unlikely (unreddened flux ratio Hγ/H $\beta = 0.46$ to 0.47 for Case B recombination at $T = 10{,}000$ K; Osterbrock 1989). No significant emission lines are found at the predicted wavelengths for these lines or others (e.g., [Ne III] or [O II]). For other plausible identifications for the apparent 5.294 μm line (e.g., Hα) we may also expect other lines that are not seen (like Hβ and [O III]), and the observed Lyα break would start to be inconsistent with the implied z in that scenario. If the 1.3 μm break were a Balmer break at $z \approx 2.5$ then the apparent line would have a rest-frame wavelength $\approx$1.5 μm, where no strong features are expected. Moreover, the possibilities of this line being Paα or Paβ at $z \approx 1.8$ or $z \approx 3.1$, respectively, would imply a location of the Balmer break that is inconsistent with the measured dropout in the spectrum. We conclude that this apparently strong, truncated emission line at the red limit of the spectrum seems inconsistent with other evidence and may be spurious.

For object CEERS_35590, a less significant emission feature (peak S/N = 3.5 for a 4 pixel extraction; smaller for a narrower extraction) is found at 5.277 μm, a few pixels short of the red limit of the spectrum. Following the same reasoning as for CEERS_99715, no other emission lines are significantly detected at wavelengths predicted under various assumed line identifications, but this is less constraining given the low S/N of the 5.277 μm feature and its larger deviation from the spatial center of the continuum trace in the 2D spectrum.

It is hard to measure precise redshifts of these two sources from breaks alone given the low S/Ns of the spectra. For CEERS_99715, the best solutions obtained with the different Lyα break fitting methods are in good agreement with each other (see Table 1). As a result, as discussed in Section 3.1, we adopt the result from the "modified EAZY" method, which gives a Lyα break fit ($z = 9.77^{+0.37}_{-0.29}$) as our best redshift for

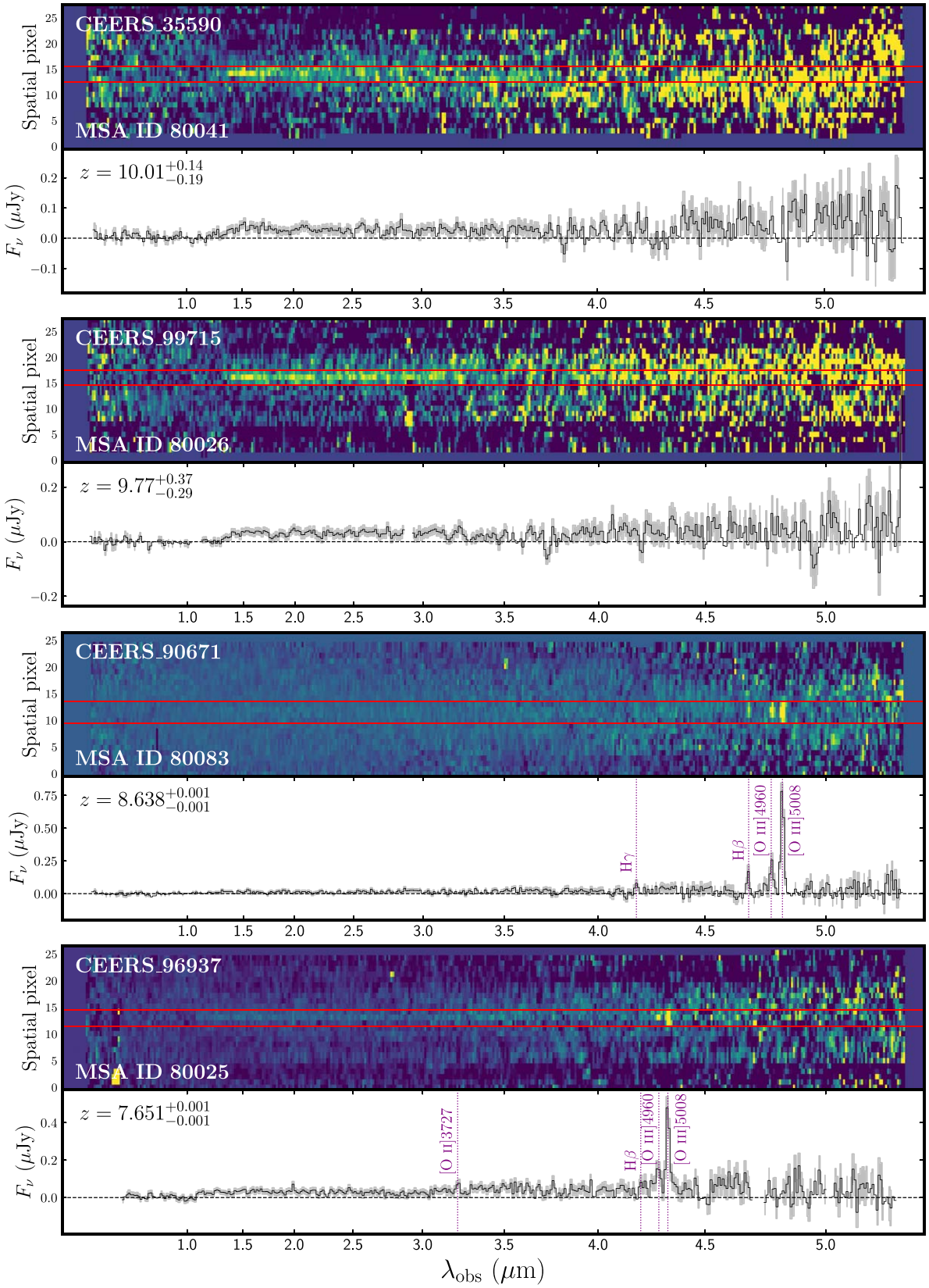

Figure 3. NIRSpec 2D (upper panels) and 1D (lower panels) prism spectra of the confirmed $z \gtrsim 8$ galaxies. Emission lines are marked with dotted purple lines when present. The red horizontal lines indicate the limits employed for the 1D extraction.

CEERS_99715. In the case of CEERS_35590, the best solutions derived from the three Lyα break fitting methods described in Section 3.1 are more discrepant and inconsistent with the photometric redshift estimate. Moreover, if this source were actually at $z \approx 8.4$–9.2 and considering the detection of strong UV continuum with a blue spectral slope (see

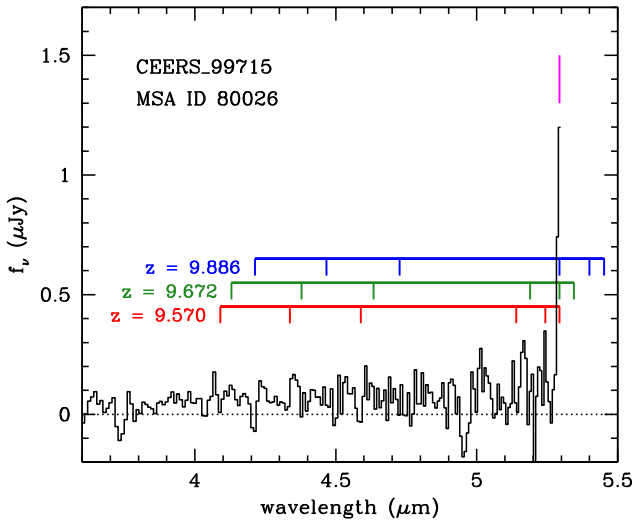

Figure 4. The red end of the extracted 1D spectrum for CEERS_99715. The last two pixels show elevated signals that could be interpreted as a truncated emission line, marked by the magenta line at 5.294 μm. The blue, green, and red bars indicate the expected locations of emission lines (from left to right: [Ne III] 3870 Å, Hδ, Hγ, Hβ, [O III] 4960 Å, and [O III] 5008 Å) at the labeled redshifts under the assumption that the possible line is [O III] 5008 Å, [O III] 4960 Å, or Hβ, respectively.

Section 3.4), we would expect [O III] 4960, 5008 Å and Hβ emission lines to be unambiguously detected at $\lambda \approx 4.6$–5.1 μm, but these lines are not observed. The best solution ($z = 10.01^{+0.14}_{-0.19}$) obtained when applying the "modified EAZY" method to the full NIRSpec spectrum (not just the break region) is in much better agreement with both the photometric redshift, the location of the Lyα break, and the absence of emission lines, which shift beyond the red wavelength limit of NIRSpec. We therefore adopt the result from the "modified EAZY" fit to the full spectrum as our best redshift for this object. This value is also consistent with a secondary peak in the redshift probability distribution function $P(z)$ derived by the MCMC1 break fitter, and is within the allowable range of $P(z)$ for MCMC2. A closer look at the Lyα breaks of these two sources with their preferred break redshift fits is shown in Figure 5.

In any case, we caution about the uncertainties associated with the exact redshift estimation of $z > 9.6$ galaxies under low-S/N conditions. In particular, bright pixels due to unremoved artifacts such as detector flaws, cosmic rays, or "snowballs" can have a large impact on break fitting if such pixels occur below the break wavelength. They can drive a break-fitting algorithm to lower-redshift values in order to accommodate these few apparently significant pixels in the spectrum.

3.1.2. The High-redshift Prism Sample

After removing the three undetected $z > 8$ candidates, we end up with a sample of four NIRCam-selected $z \gtrsim 8$ galaxies in CEERS epoch 3 observations. The two at $z < 9$ present clear emission lines (see Figure 3) and therefore robust spectroscopic redshifts. For the two at $z \sim 10$, their spectra strongly suggest a high-z nature in agreement with their original photometric redshift estimates, but their exact redshifts are hard to determine given the absence of clear emission lines and the systematics in the redshift measured from the continuum break. Hence, the redshifts derived for these two sources present larger uncertainties. However, the detected breaks and the absence of definitive emission lines in the NIRSpec spectral range support the inferred redshifts $z > 9.6$. The adopted spectroscopic redshifts for the NIRCam-selected $z > 8$ candidates observed with NIRSpec in CEERS epoch 3 are summarized in Table 2. Information about the three spectroscopically undetected targets is presented in Appendix A along with all the other CEERS $z > 8$ candidates in NIRSpec MSA observations without a robust redshift measurement (see Arrabal Haro et al. 2023; Fujimoto et al. 2023).

3.2. Emission Line Measurements

For the two galaxies with $7.5 < z < 9$ we measure observed-frame equivalent widths (EWs) of the emission lines by fitting each 1D spectrum with a composite "line+continuum" model. Each line is modeled with a 1D Gaussian. The amplitude, spectral width, and center of the Gaussian are left as free parameters. The width (σ) is allowed to vary from 50 to 400 km s^{-1} and the line center is allowed to vary over –600 to +600 km s^{-1} from the systemic redshift of the galaxy. The continuum is modeled using a 1D polynomial (i.e., a line with a slope). To derive uncertainties on the fitted parameters, we adopt a Monte Carlo approach and create 1000 realizations of each 1D spectrum. The realizations are created by perturbing the observed spectrum by its error spectrum. For each realization, we refit the composite model. We estimate the uncertainties on the line fluxes and the level of the continuum from the distribution of the best-fit parameters of the suite of realizations.

The rest-frame EWs of the emission lines detected are listed in Table 3. There is no evidence of Lyα emission in any of the four sources presented in this work.

3.3. SED Fitting

We carry out SED modeling using three independent fitting tools: BAGPIPES (Carnall et al. 2018, 2019b), CIGALE (Burgarella et al. 2005; Noll et al. 2009; Boquien et al. 2019), and Dense Basis (Iyer et al. 2019). For the sources with clear [O III] emission, the redshift is fixed to the adopted spectroscopic value (Table 2) during the fitting. For the two $z \sim 10$ galaxies, Gaussian redshift priors are allowed with a σ similar to the larger uncertainty on the Lyα break redshifts. The SED fitting performed with CIGALE and Dense Basis only makes use of the NIRCam photometry, while the spectra are also included when using BAGPIPES. In all cases, we assume a Chabrier (2003) initial mass function (IMF).

All sources are fit with BAGPIPES assuming a Calzetti et al. (2000) dust law. We fit with BPASS v2.2.1 (Eldridge et al. 2017) stellar templates over a range of ionization parameter $\log U \in [-4, -1]$ and total (stellar and gas-phase) metallicity $Z \in [-3, 1]$, a flexible star formation history (SFH) represented by a Gaussian mixture model (GMM; Iyer et al. 2019) and a log-normal prior on the star formation rate (SFR) over the range $\log(\mathrm{SFR}) \in [-2, 3]$. We first scale the individual spectra to match the observed photometry for each source, then fit the source photometry and spectra simultaneously, assuming a χ^2-likelihood function, to infer galaxy properties from the posterior distributions. When fitting CEERS_35590 we include the MIRI F560W and F770W photometry (Section 2.2). To determine if the inclusion of the MIRI photometry has any impact on the inferred stellar mass and SFR for CEERS_35590,

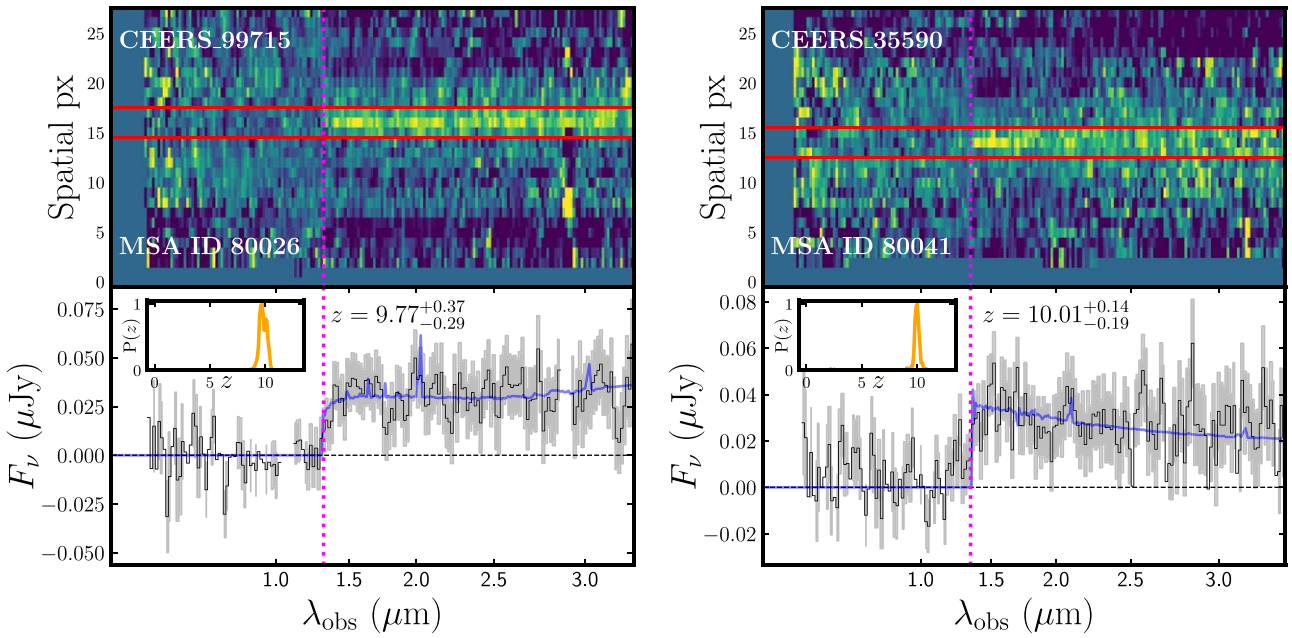

Figure 5. 2D (top) and 1D (bottom) spectra of CEERS_99715 (left) and CEERS_35590 (right). The wavelength axes have been limited to visualize the Lyα break better. The bottom panel inset shows the redshift probability distribution function. The best-fitting EAZY model is represented in blue, with a dotted vertical magenta line extending the derived Lyα break location to the 2D spectrum. The two horizontal red lines in the 2D spectrum indicate the 1D extraction window. The shaded gray area corresponds to the rescaled 1D flux errors (see Appendix B).

Table 2
Adopted Spectroscopic Redshifts of the CEERS Epoch 3 NIRCam-selected $z > 8$ Candidates

Source ID (1)	MSA ID (2)	$z_{\rm spec}$ (3)	Method (4)
CEERS_35590	80041	$10.01^{+0.14}_{-0.19}$	EAZY-full
CEERS_99715	80026	$9.77^{+0.37}_{-0.29}$	EAZY-break
CEERS_90671	80083	$8.638^{+0.001}_{-0.001}$	[O III]
CEERS_96937	80025	$7.651^{+0.001}_{-0.001}$	[O III]

Note. (1) Source ID in the CEERS catalog (S. L. Finkelstein et al. 2023, in preparation). (2) Source ID in the CEERS MSA observations. (3) Best spectroscopic redshift. (4) Redshift estimation method (see Section 3.1). The estimation based on [O III] 5008 Å is prioritized in the cases where that line is detected. In the absence of high S/N emission lines, the EAZY fit is to the Lyα break or to the complete spectrum when the break S/N is too low for a robust estimation.

Table 3
EW$_0$ for the Lines Detected in the Prism Spectra

MSA ID	[O II] 3727 Å	Hγ	Hβ	[O III] 4960 Å	[O III] 5008 Å
			(Å)		
(1)	(2)	(3)	(4)	(5)	(6)
80083	—	44^{+27}_{-19}	56^{+31}_{-23}	81^{+30}_{-18}	287^{+68}_{-44}
80025	57^{+30}_{-28}	—	8^{+18}_{-8}	51^{+17}_{-21}	187^{+27}_{-23}

Note. (1) Source ID in the CEERS MSA observations. (2)–(6) Rest-frame EWs of the different emission lines.

we fit the CEERS_35590 photometry and spectrum a second time, but exclude the MIRI photometry. In both cases, we infer a stellar mass of $\log(M_*/M_\odot) = 9.1 \pm 0.1$ and $\log(\mathrm{SFR}) = 9 \pm 2$ and therefore adopt the fit that includes the MIRI photometry as the best-fitting Bagpipes model.

Similarly, sources are fit with the Dense Basis SED fitting code using flexible nonparametric SFHs (Iyer et al. 2019). For this work, we define three "shape" parameters that describe the SFH: t_{25}, t_{50}, and t_{75} (requiring the recovered SFH of the galaxy to form "x" fraction of its total mass by time t_x). We impose a uniform (flat) prior on the specific star formation rate (sSFR) with limits on the SFR ($\mathrm{SFR}/M_\odot\ \mathrm{yr}^{-1} \in [10^{-2}, 10^3]$), an exponential prior on the dust attenuation over a wide range of values ($A_V \in [0, 4]$), and a uniform (in log-space) prior on the metallicity ($Z/Z_\odot \in [0.01, 2.0]$).

Finally, we fit the objects with CIGALE. We select a delayed SFH with SFR $\propto t \times \exp(-t/\tau)$. An additional final burst of star formation ($k \times \exp(-t/\tau_{\rm burst})$) is introduced if it provides a better fit. The age of the main stellar population $\mathrm{age}_{\rm main}$ is allowed to vary from 2 Myr to 1 Gyr while $\mathrm{age}_{\rm burst}$ is set to 1 Myr and the burst fraction ($f_{\rm burst} \equiv M_{\star,\rm burst}/M_{\star,\rm tot}$) is free in the range $f_{\rm burst} \in [0, 0.5]$. BPASS v2.2.1 stellar templates with a fixed $Z = 0.008$ metallicity are used. Dust attenuation following Calzetti et al. (2000) is applied to the stellar continuum, while nebular emission (continuum and lines) is attenuated with a screen model and a Small Magellanic Cloud (SMC) extinction curve (Pei 1992).

The main physical parameters derived for our four objects with each SED fitting tool are summarized in Table 4, and the SEDs and best-fitting models of the two $z \sim 10$ objects are presented in Figure 6.

The MIRI photometric measurements for CEERS_35590 have low S/N = 1.7 and 2.9 for F560W and F770W, respectively, but both measurements (especially F770W) are well above a simple extrapolation of the NIRCam photometry to $\lambda > 5\ \mu$m (see Figure 6). They are consistent with the presence of strong [O III]+Hβ emission in F560W and Hα+[N II] in F770W.

Furthermore, an additional fit of the two $z \sim 10$ sources is carried out with BAGPIPES making use of the photometry and spectra in the same way described above but without imposing

Table 4
Stellar Mass, SFR, sSFR, and Dust Attenuation

Code	MSA ID	$\log(M_*/M_\odot)$	SFR ($M_\odot$ yr^{-1})	sSFR log(yr^{-1})	A_V (mag)
(1)	(2)	(3)	(4)	(5)	(6)
B	80041	$9.1^{+0.1}_{-0.1}$	9^{+2}_{-2}	$-8.2^{+0.1}_{-0.2}$	$0.1^{+0.1}_{-0.1}$
	80026	$9.5^{+0.1}_{-0.1}$	6^{+4}_{-2}	$-8.7^{+0.3}_{-0.3}$	$0.1^{+0.1}_{-0.1}$
	80083	$8.8^{+0.1}_{-0.1}$	3^{+2}_{-2}	$-8.3^{+0.2}_{-0.4}$	$0.4^{+0.2}_{-0.2}$
	80025	$9.3^{+0.1}_{-0.1}$	6^{+1}_{-1}	$-8.5^{+0.2}_{-0.2}$	$0.4^{+0.1}_{-0.1}$
C	80041	$8.2^{+0.2}_{-0.4}$	6^{+4}_{-4}	$-7.4^{+0.6}_{-0.7}$	$0.1^{+0.1}_{-0.1}$
	80026	$9.0^{+0.2}_{-0.3}$	11^{+15}_{-11}	$-7.9^{+0.6}_{-1.2}$	$0.4^{+0.3}_{-0.3}$
	80083	$8.2^{+0.2}_{-0.4}$	8^{+7}_{-7}	$-7.3^{+0.7}_{-1.1}$	$0.9^{+0.4}_{-0.4}$
	80025	$8.8^{+0.1}_{-0.2}$	8^{+10}_{-8}	$-7.9^{+0.6}_{-1.0}$	$0.6^{+0.3}_{-0.3}$
DB	80041	$8.7^{+0.4}_{-0.3}$	3^{+21}_{-1}	$-8.2^{+1.2}_{-0.6}$	$0.1^{+0.2}_{-0.1}$
	80026	$9.2^{+0.2}_{-0.4}$	9^{+4}_{-4}	$-8.3^{+0.6}_{-0.5}$	$0.1^{+0.2}_{-0.1}$
	80083	$8.8^{+0.0}_{-1.0}$	1^{+1}_{-1}	$-8.7^{+1.0}_{-0.9}$	$0.5^{+0.3}_{-0.3}$
	80025	$8.6^{+0.1}_{-0.1}$	$0.4^{+11}_{-0.3}$	$-9.4^{+2.0}_{-0.4}$	$0.0^{+0.1}_{-0.0}$

Note. (1) SED fitting code used to derive the physical properties (B: BAGPIPES, C: CIGALE, DB: Dense Basis). (2) Source ID in the CEERS MSA observations. (3) Stellar mass. (4) SFR averaged over the last 100 Myr. (5) sSFR. (6) Stellar dust extinction.

any constraints on the redshift. The best redshift solutions obtained in this case are $z = 9.72^{+0.06}_{-0.04}$ for CEERS_99715 and $z = 9.97^{+0.10}_{-0.07}$ for CEERS_35590, in very good agreement with our adopted fiducial values (see Table 2).

3.4. UV Spectral Slope

We measure the UV spectral slope β from the photometry, the spectra, and the best-fitting SED models using the adopted redshifts in Table 2.

For the photometry, we fit the WFC3 and NIRCam SED with a power law ($f_\lambda \propto \lambda^\beta$) between rest-frame 1500 and 3000 Å (see Calzetti et al. 1994). Using the EMCEE software (Foreman-Mackey et al. 2013), we measure the posterior distribution on β and obtain the median and 68% central width from the posterior. The same process is employed to measure the β slope directly from the prism spectra. We note here that the comparison of the spectral flux density with the photometry of the four objects here presented reveals small flux discrepancies (by a factor <2), but these deviations are similar along the prism wavelengths without any particular trend, so we expect the spectroscopic β not to be significantly affected by the absence of a precise slit loss correction. The model-derived β is retrieved from the best BAGPIPES models resulting from the SED fitting employing both photometry and spectra (see Section 3.3).

The absolute UV magnitude $M_{\rm UV}$ at 1500 Å is estimated following the methodology used in Finkelstein et al. (2015). Table 5 presents the β values obtained from the three different estimations as well as the $M_{\rm UV}$ values for our four galaxies.

3.5. Morphology

We use `Galfit` (Peng et al. 2002, 2010), a least-squares fitting algorithm that finds the optimum Sérsic fit to a galaxy's light profile, to measure the size and morphology of the four spectroscopically confirmed $z > 8$ galaxies listed in Table 1. As input, we create 100×100 pixel cutouts of the F200W and F277W images (with a 0.″03 pixel scale), the error array to be used as the input sigma image, and the source segmentation map. We use empirically derived PSFs based on stacked stars from the image. As an initial guess of the parameters we use the source location, magnitude, size, position angle, and axis ratios from the `Source Extractor` (Bertin & Arnouts 1996) catalog. We then run `Galfit`, allowing the Sérsic index to vary between 0.01 and 8, the magnitude of the galaxy between 0 and 45, the size (R_e) between 0.3 and 200 pixels, and allowing the PSF to be oversampled by a factor of 9. To make sure the fits were reasonable, we then visually inspect the best-fit model and image residual.

In F277W, CEERS_35590 is well resolved and fit with a single Sérsic component. We measure a half-light radius of 3.31 ± 0.18 pixels (0.42 ± 0.02 kpc) with a Sérsic index of $n = 0.75$. In F200W, `Galfit` hits the constraint limits, indicating that the source is not well fit. Visually, CEERS_35590 is very compact in F200W and more extended at longer wavelengths with what appears to be extended faint emission in F356W and F444W to the east of the galaxy (see Figure 7).

CEERS_99715 is well resolved in both F200W and F277W and we are able to fit both filters with a single Sérsic component. The source has different visual morphologies in F200W and F277W, with two components visible at shorter wavelengths (see Figure 7). In F200W we measure a half-light radius of 4.53 ± 0.19 pixels (0.58 ± 0.02 kpc) with $n = 0.60$ and in F277W we measure a half-light radius of 4.86 ± 0.17 pixels (0.62 ± 0.02 kpc) with $n = 0.77$.

CEERS_90671 is unresolved in F200W and marginally resolved in F277W with a half-light radius of 2.86 ± 0.22 pixels (0.36 ± 0.03 kpc) and $n = 0.68$. CEERS_96937 is well resolved in F277W, with a half-light radius of 16.50 ± 2.64 pixels (2.09 ± 0.34 kpc) and $n = 2.53$. In F200W, the fit is likely affected by what appears to be a snowball artifact. We measure a half-light radius of 4.07 ± 0.76 pixels (0.52 ± 0.10 kpc) and $n = 0.61$.

4. Results and Discussion

4.1. Physical Properties

The main physical properties derived through SED fitting for the four spectroscopically confirmed galaxies are summarized in Table 4. Clear differences can be appreciated in the values derived from each SED fitting code for some sources, as expected when the SFH cannot be well constrained at high-z (see, e.g., Carnall et al. 2019a; Leja et al. 2019; Pacifici et al. 2023). These differences illustrate the difficulty of determining stellar population parameters even at this very early cosmic epoch when galaxy ages are necessarily young. In particular, we obtain systematically higher A_V (although compatible within the errors) from the CIGALE fitting, as well as lower stellar masses.

In this section we focus on the physical properties of the two $z \sim 10$ sources presented in this work, referring to Fujimoto et al. (2023) and P. Arrabal Haro et al. (2023, in preparation) for a more general discussion of the complete CEERS $z = 8$–9 spectroscopic sample. The confirmation of these two objects raises to six the number of spectroscopically confirmed luminous sources with $M_{\rm UV} < -20$ at $z \gtrsim 10$, the others being GN-z11 (Oesch et al. 2016; Bunker et al. 2023; Tacchella et al. 2023), Maisie's galaxy (Finkelstein et al. 2022;

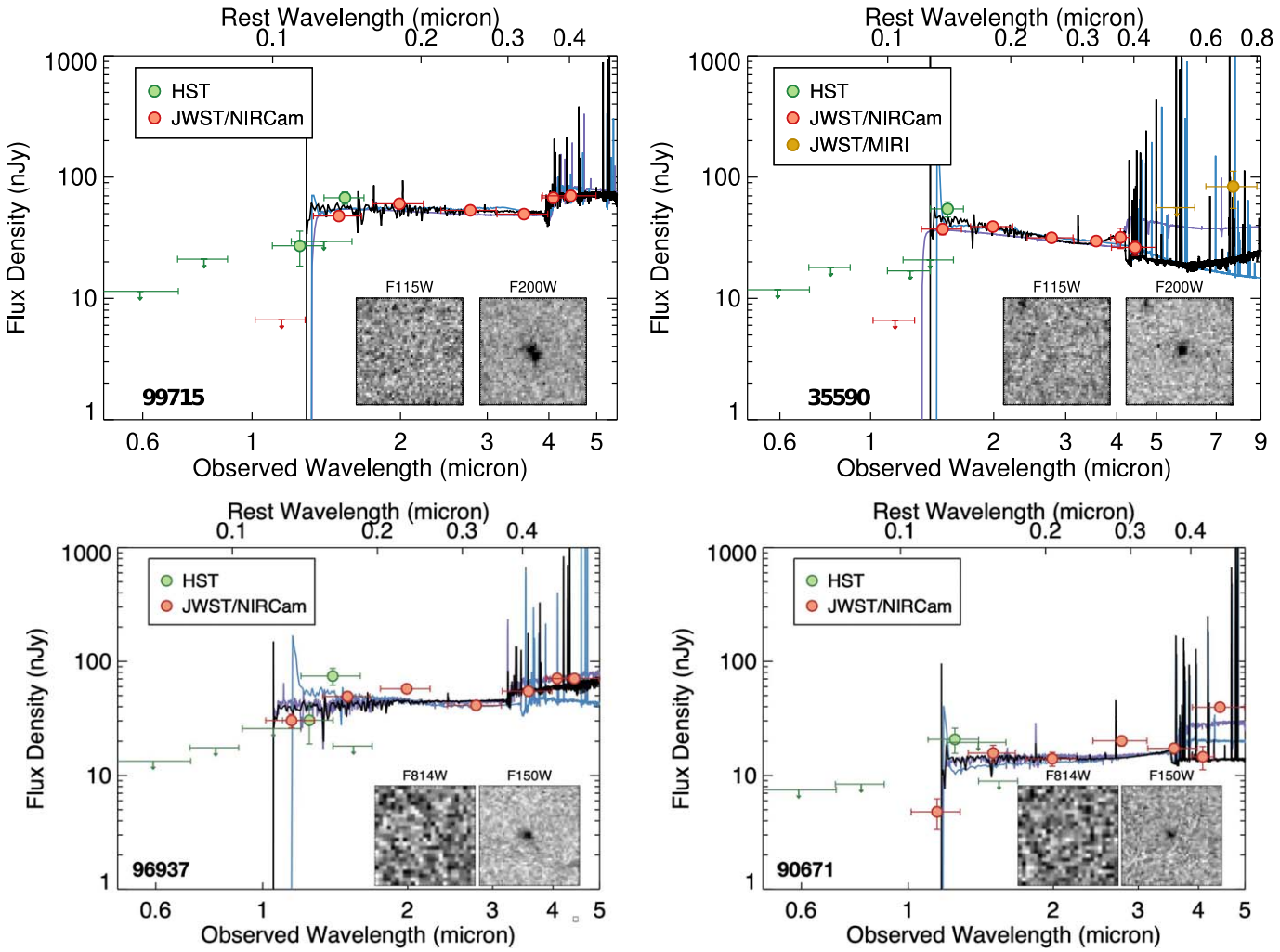

Figure 6. SEDs of the four spectroscopically confirmed sources. The measured photometry in ACS F606W and F841W filters is represented in green; NIRCam F115W, F150W, F200W, F277W, F356W, F410M, and F444W, in red; and MIRI F560W and F770W (for CEERS_35590 only), in orange. The spectra represent the best-fitting stellar population models, with black, blue, and purple representing CIGALE, DENSE BASIS, and BAGPIPES, respectively. The inset stamps are $1\farcs5 \times 1\farcs5$ cutouts of some combination of the NIRCam F115W, F150W, and F200W and ACS F814W images, highlighting the emission drop corresponding to the Lyα break.

Table 5
$M_{\rm UV}$ and Independent UV β Slopes

MSA ID (1)	$M_{\rm UV}$ (2)	$\beta_{\rm phot}$ (3)	$\beta_{\rm model}$ (4)	$\beta_{\rm spec}$ (5)
80041	$-20.1^{0.1}_{0.1}$	$-2.19^{+0.92}_{-0.56}$	$-2.33^{+0.06}_{-0.06}$	$-1.93^{+0.55}_{-0.52}$
80026	$-20.5^{0.1}_{0.1}$	$-2.16^{+0.78}_{-0.52}$	$-2.15^{+0.05}_{-0.05}$	$-1.87^{+0.54}_{-0.52}$
80083	$-18.7^{0.1}_{0.1}$	$-1.45^{+0.74}_{-0.71}$	$-1.90^{+0.17}_{-0.20}$	$-1.57^{+0.37}_{-0.46}$
80025	$-20.0^{0.2}_{0.1}$	$-2.32^{+0.93}_{-0.48}$	$-1.59^{+0.08}_{-0.08}$	$-1.86^{+0.57}_{-0.56}$

Note. (1) Source ID in the CEERS MSA observations. (2) Absolute UV magnitude measured at rest-frame 1500 Å. (3) Photometric UV slope. (4) UV slope derived from the BAGPIPES models best-fitting photometry and spectra simultaneously. (5) Spectroscopic UV slope.

Arrabal Haro et al. 2023), CEERS_11384 (Arrabal Haro et al. 2023; Harikane et al. 2023a), and M0647-JD (Harikane et al. 2023a; Hsiao et al. 2023). This suggests that these luminous sources appeared more often than expected early in the history of the universe (<500 Myr).

The stellar masses derived are among the largest of those reported in Arrabal Haro et al. (2023), Bunker et al. (2023), Curtis-Lake et al. (2023), and Roberts-Borsani et al. (2023) for spectroscopically confirmed $z \gtrsim 10$ galaxies. While we cannot robustly constrain the stellar mass of CEERS_35590 ($\log(M_\star/M_\odot) \simeq 8.2$–$9.1$), we find a relatively high $\log(M_\star/M_\odot) \simeq 9.0$–$9.5$ for CEERS_99715 (see Table 4), similar to those of GN-z11 and GS-z11-0 (Curtis-Lake et al. 2023; Robertson et al. 2023). Considering the still limited spectroscopic follow up of $z > 10$ candidates to date, the confirmation of already three objects with $\log(M_\star/M_\odot) \geqslant 9$ suggests that the abundance of such evolved systems is higher than predicted (e.g., Finkelstein et al. 2022, 2023; Harikane et al. 2023b), although it is important to keep in mind that these are the easiest sources to detect among the $z > 10$ candidates. Nevertheless, the Santa Cruz semianalytic model (SC SAM; e.g., Somerville et al. 2015, 2021) predicts 0.3^{+2}_{-0} galaxies with $\log(M_\star/M_\odot) \sim 9$ at $9.48 < z < 10.15$ (defined to account for our z errors) in the whole NIRCam imaging area covered by CEERS (see Yung et al. 2019b). Although confirming a single galaxy under those conditions (and a tentative one) is still consistent within the uncertainties of the prediction, it is likely that the actual number of galaxies at those redshifts and stellar mass is larger if we consider that the MSA observations presented here are a lower limit for any kind of number density estimation. Similarly, the SC SAM predicts $1.1^{+2.7}_{-0.4}$ sources with

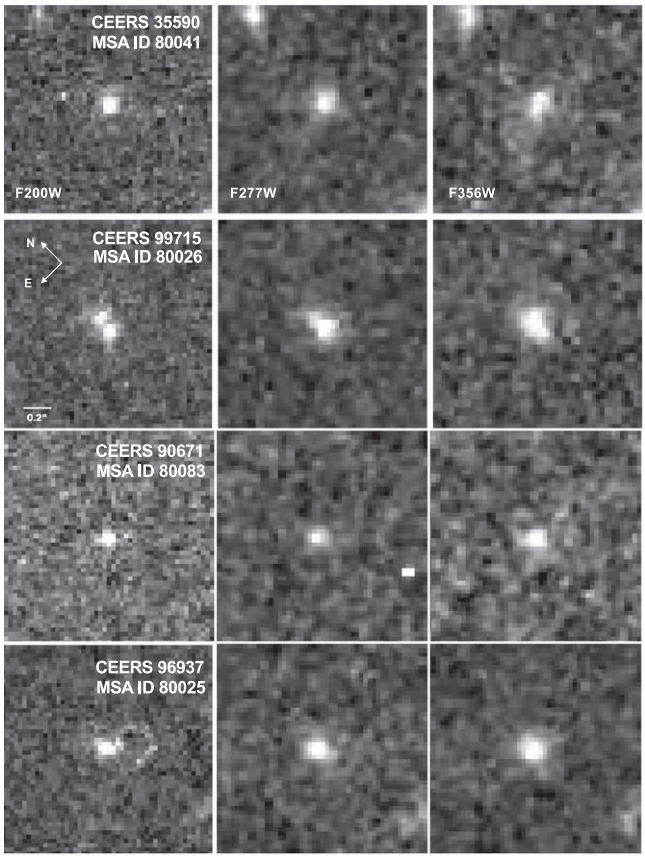

Figure 7. Cutout images of the four $z > 8$ sources in F200W, F277W, and F356W, highlighting the morphological structure visible at different wavelengths. Each cutout is $1\farcs5 \times 1\farcs5$.

$M_{\rm UV} \sim -20.5$ at the same redshifts (Yung et al. 2019a), again still compatible with the lower limit of two objects here presented, but likely underpredicting the actual number when we consider the small fraction of spectroscopic follow up of the CEERS field. Predictions from the SIMBA-EoR hydrodynamic simulation (Davé et al. 2019) indicate that we should see $\sim$1 galaxy at $8 < z < 10$ with SFR $> 3\,M_\odot\,{\rm yr}^{-1}$, highly inconsistent with the lower limit of 4–6 (depending on the assumed SFH during SED fitting) already reported in Fujimoto et al. (2023) and this work. Reducing stellar feedback in the simulations (see, e.g., Dekel et al. 2023; Yung et al. 2023) raises the number of expected galaxies in the SIMBA-EoR simulation to $\sim$7, again leaving not much room before the observations are in tension with even the no-feedback simulations.

The low dust attenuation measured for the two $z \sim 10$ sources $A_V \simeq 0.1^{+0.2}_{-0.1}$ is in very good agreement with similarly low values ($A_V \leqslant 0.3$) reported for all the confirmed $z \gtrsim 10$ objects in the literature (Arrabal Haro et al. 2023; Hsiao et al. 2023; Robertson et al. 2023; Tacchella et al. 2023), often compatible with zero attenuation within the errors. This is interesting as a hypothetical scenario with negligible dust attenuation could be one of the factors that would increase the predicted numbers of bright galaxies in the early universe in some theoretical models (Ferrara et al. 2023). Consistent with the low dust extinctions measured, the spectra of the two $z \sim 10$ galaxies present blue continua, although not extremely blue, with $-2.3 \lesssim \beta \lesssim -1.9$ for the independent estimations (see Table 5).

Finally, we measure compact sizes for the two $z \sim 10$ objects, with half-light radius $\sim$0.4−0.6 kpc, consistent with sizes previously measured for objects at the EoR (see, e.g., Mascia et al. 2023; Treu et al. 2023). Interestingly, we see some variation of the global morphology of both sources with wavelength, contrary to the observed behavior in Treu et al. (2023). In particular, the two resolved components observed for CEERS_99715 at the shorter wavelengths present an interesting case study for future resolved SED fitting analyses that could help distinguish whether this is a merger of two distinct galaxies, or if they are two "clumps" within one galaxy with spatially distinct regions of star formation or separated by a dust lane. If this is an ongoing merger it may illustrate the processes that lead to early galaxies as massive as CEERS_99715 ($\log(M_\star/M_\odot) \simeq 9.3^{+0.2}_{-0.3}$; average from the three independent estimations), as discussed in Boyett et al. (2023).

4.2. Robustness of Photometric Redshifts

The CEERS epoch 3 NIRSpec observations presented here complete the Cycle 1 spectroscopic follow up of $z > 8$ galaxy candidates in the CEERS field. Here we consider the CEERS NIRSpec observations together with one additional NIRSpec field observed in DD time program #2750 (PI: P. Arrabal Haro), which also targeted CEERS NIRCam-selected high-redshift candidates using longer exposure times (18,387 s, compared to 3107 s for CEERS). Together, these NIRSpec MSA observations targeted 32 candidates that meet the $z > 8$ photometric redshift selection criteria of Finkelstein et al. (2023). Merging the spectroscopic measurements from Arrabal Haro et al. (2023), Fujimoto et al. (2023), Tang et al. (2023), and from the present work, 24 out of the 32 targets have robust spectroscopic redshifts.

Eight targets meeting the Finkelstein et al. (2023) $z_{\rm phot}$ criteria do not have securely measured spectroscopic redshifts. Seven of these eight objects are faint ($m_{\rm F277W} \gtrsim 28$) and have $z_{\rm phot} > 10$, where strong emission lines would not be expected at $\lambda < 5.3\,\mu$m and where the continuum S/N is low with the exposure times employed for the CEERS NIRSpec observations. None of these eight candidates shows emission lines that would be expected if they were at $z \lesssim 9.6$ (see also Fujimoto et al. 2023). Therefore, it seems likely that these galaxies have $z > 9.6$, despite the lack of secure spectroscopic confirmation.

Several other authors have also identified high-redshift galaxy candidates from CEERS NIRCam data using different selection criteria. Some of those candidates have also been observed with NIRSpec, including two targeted but undetected sources from Donnan et al. (2023) and Whitler et al. (2023), plus a third $z \sim 8$ candidate from Labbé et al. (2023) with spectroscopic $z = 5.623$ (Kocevski et al. 2023). In total, 35 CEERS $z > 8$ candidates from the literature have been followed up with NIRSpec MSA observations, 25 of them with robust spectroscopic redshift measurements.

Appendix A presents a complete census of spectroscopically observed $z_{\rm phot} > 8$ candidates in CEERS from Endsley et al. (2022), Bouwens et al. (2023), Donnan et al. (2023), Finkelstein et al. (2023), Harikane et al. (2023b), Labbé et al. (2023), and Whitler et al. (2023). For completeness, we include one object with a lower photometric redshift ($z_{\rm phot} = 6.45$) that is unambiguously confirmed to have spectroscopic $z = 8.175$ (MSA ID 1149; Heintz et al. 2023; Sanders et al. 2023; Tang et al. 2023).

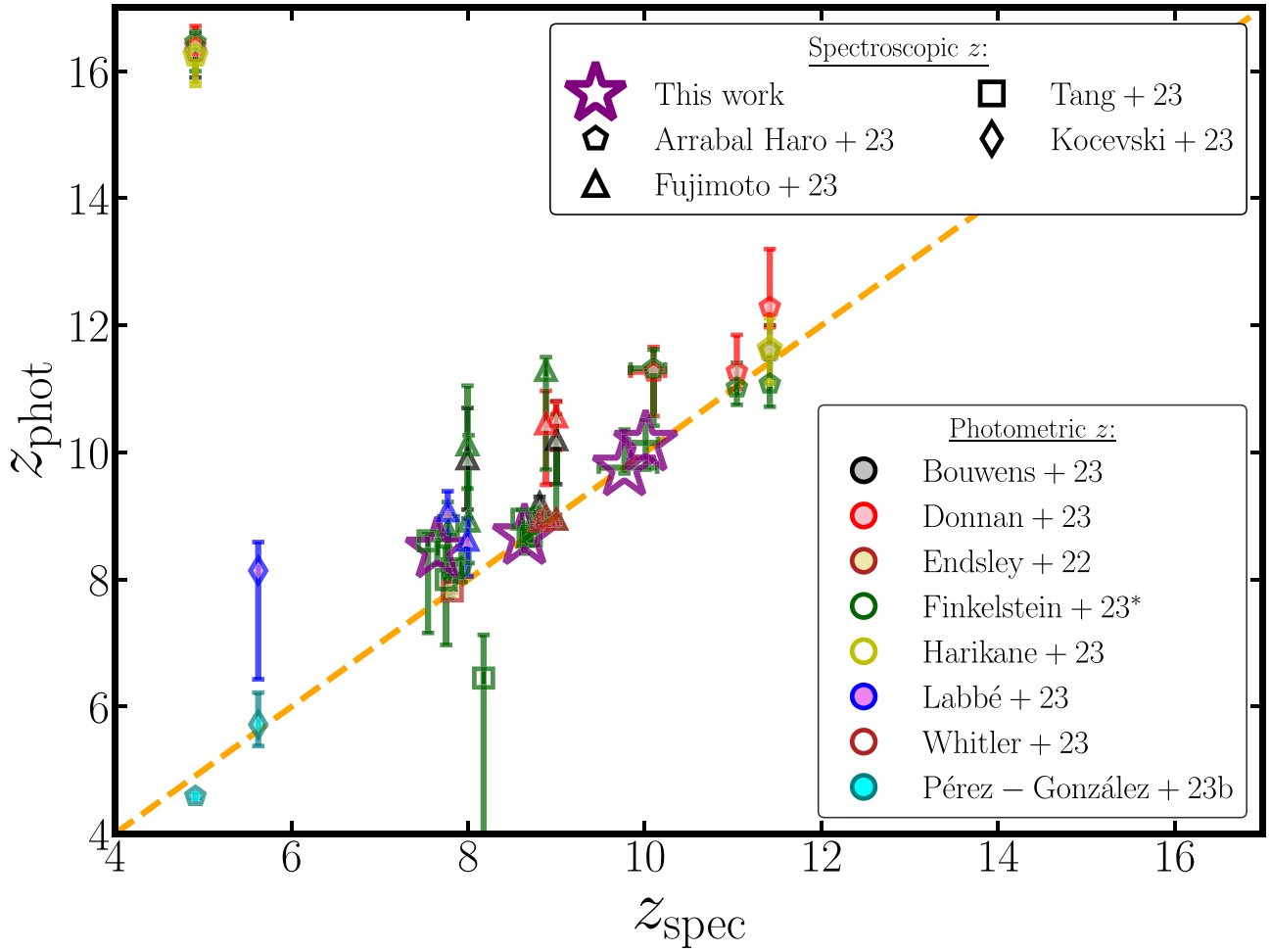

Figure 8. Comparison of photometric and spectroscopic redshifts for $z_{\rm phot} > 8$ candidates in CEERS from Endsley et al. (2022), Bouwens et al. (2023), Donnan et al. (2023), Finkelstein et al. (2023), Harikane et al. (2023b), Labbé et al. (2023), and Whitler et al. (2023) with secure spectroscopic redshifts from the complete NIRSpec data in the EGS field. The green markers correspond to galaxies in Finkelstein et al. (2023) or selected using the selection criteria employed in that work (see Section 2.1). For completeness, photometric estimations from the $2 \lesssim z \lesssim 7$ sample in Pérez-González et al. (2023a) for the two lower-z interlopers are also included. The spectroscopic redshifts are remeasured here for galaxies with emission lines spectroscopically reported in Arrabal Haro et al. (2023), Fujimoto et al. (2023), Kocevski et al. (2023), and Tang et al. (2023). The four galaxies presented in this work for the first time are highlighted with purple stars. The one-to-one relation is shown as a dashed orange line. Note that several of the points represented in this figure correspond to independent photometric estimations of the same galaxies (therefore at the same $z_{\rm spec}$ value). A complete compilation of the redshifts here presented can be found in Appendix A.

A comparison of the spectroscopic and photometric redshifts for these high-redshift candidates is presented in Figure 8. This includes objects spectroscopically confirmed in Arrabal Haro et al. (2023), Fujimoto et al. (2023), Kocevski et al. (2023), and Tang et al. (2023), whose redshifts have been remeasured for consistency, following the methodology described for emission line redshifts in Section 3.1. The good redshift agreement overall suggests that photometric high-z selection methods perform quite well at identifying these sources. Out of the 25 galaxies with robust spectroscopy, only two (8%) are demonstrated to be lower-redshift interlopers. The first of these sources is CEERS_24015, originally selected as a massive $z \sim 8$ candidate in Labbé et al. (2023) and later confirmed as a low-luminosity active galactic nucleus at $z = 5.623$ by Kocevski et al. (2023). The other interloper is CEERS_13256, originally included in several high-z selections (Bouwens et al. 2023; Donnan et al. 2023; Finkelstein et al. 2023, Harikane et al. 2023b) and recently confirmed at $z = 4.91$ by Arrabal Haro et al. (2023). It is worth noting that both of these interlopers were also assigned lower photometric redshifts (consistent with their spectroscopic values) by other authors (see, e.g., Pérez-González et al. 2023a; and the discussions in Naidu et al. 2022a; Zavala et al. 2023). This demonstrates that even the few confirmed interlopers can be photometrically identified under certain selection criteria.

It is important to note that the high-z photometric samples discussed here are not merely defined by the most likely redshift values from template fitting; they also meet additional color and χ^2 criteria that are used to define a high-fidelity sample (see, e.g., the detailed discussion in Finkelstein et al. 2023). In Appendix C we show an illustrative example of a galaxy whose photometric redshift $P(z)$ peaks at $z_{\rm best} > 8$, but which does not meet the other high-z selection criteria of Finkelstein et al. (2023), and for which NIRSpec measures $z = 5.271$. Objects like this could appear more frequently in high-z photometric samples with more relaxed selection criteria. Therefore, the high confirmation rate (92% among the detected targets) we find in this work can only be extrapolated to other high-z samples based on selection criteria similar to the ones employed in the studies analyzed here and should not be taken for granted for less rigorously selected samples.

In spite of the high ratio of confirmed high-z sources, we observe a trend where the photo-z is often slightly overestimated. Considering a mean photometric redshift for each individual object among their estimations in different studies, and after removing the low-z interlopers, we compute an average deviation $\langle \Delta z \equiv z_{\rm phot} - z_{\rm spec} \rangle = 0.45 \pm 0.11$. This could, in part, be due to a confirmation bias that would cause a larger number of objects at lower redshifts to be well detected spectroscopically as they would be typically brighter. This effect would be particularly relevant at $z \gtrsim 9.6$, where strong rest-frame optical emission lines start to redshift beyond the red wavelength limit of the NIRSpec instrument, making lower spectroscopic redshifts easier to confirm via the presence of Hβ and [O III] in the spectrum. However, the same trend is observed at $z_{\rm spec} = 8$–9 where strong lines are detected with NIRSpec but where several galaxies have higher photometric redshifts. This suggests a deeper reason for this deviation.

It is also possible that there are physical differences in the true continuum shapes of very-high-z galaxy spectra which are not accounted for in the templates used for photometric redshift estimation. In any case, these results suggest that our current $z > 8$ selection criteria are good, but at the same time we might need to modify our galaxy templates to resemble the SEDs of very-high-z galaxies better and further refine our photo-z estimations. For this purpose, deep continuum spectroscopy of a variety of early galaxies will be necessary to build a proper database of templates.

All things considered, the low fraction of interlopers reported in this work for $z > 8$ candidates in CEERS (8%) is insufficient to account for the high number densities reported in several studies (Finkelstein et al. 2022; Donnan et al. 2023; Finkelstein et al. 2023; Harikane et al. 2023b) with respect to the theoretical predictions. Therefore, these spectroscopic observations, while incomplete, reinforce the photometric evidence for an abundant population of comparatively luminous galaxies at $z > 8$, extending at least to $z \simeq 10$ and perhaps beyond. For galaxies at $z > 9.6$, where the strongest rest-frame optical emission lines shift out of the NIRSpec spectral range, the 3107 s exposure times of CEERS NIRSpec observations limit redshift confirmation to brighter sources. Deeper surveys are needed to achieve higher spectroscopic completeness and to probe fainter down the galaxy luminosity function.

5. Summary

We present spectroscopic follow up of seven $z > 8$ candidates in CEERS epoch 3 NIRSpec MSA observations. Four out of the seven targets are spectroscopically detected. Two of them present clear rest-frame optical emission lines that result in unambiguous redshifts $z = 8.638$ and $z = 7.651$. The other two detected sources present clear Lyα continuum breaks, but not emission lines. We determine their redshifts by fitting the continuum break through different methods, adopting fiducial values of $z = 9.77^{+0.37}_{-0.29}$ and $z = 10.01^{+0.14}_{-0.19}$. We show that spectroscopic redshifts based only on fitting the Lyα break are effective to confirm the high-z nature of these objects, but have relatively large uncertainties, especially when working with low S/N breaks, due to the low spectral resolution of the NIRSpec prism at the bluest wavelengths. The three undetected targets do not show emission lines that identify them as lower-z interlopers, therefore they remain consistent with $z \gtrsim 9.6$ scenarios despite not having robust redshift determinations.

For the two $z \sim 10$ sources, we measure relatively high luminosities ($M_{\rm UV} < -20$), blue UV slopes ($-2.3 \lesssim \beta \lesssim -1.9$), and low dust extinction ($A_V \simeq 0.15^{+0.3}_{-0.1}$). The object CEERS_99715, in particular, presents a high stellar mass ($\log(M_\star/M_\odot) = 9.0 - 9.5$). Additionally, its morphological analysis reveals two differentiated substructures at the bluer wavelengths (NIRCam/F200W) that might be hints of a minor merger which could help to understand the way objects like this built up a relatively large stellar mass only ∼485 Myr after the Big Bang.

The spectroscopic results presented here are combined with all the available $z > 8$ spectroscopy from previous works for a complete census of NIRSpec MSA spectroscopy in the EGS field. Thirty-five targets from all the CEERS $z > 8$ photometric samples in the literature have been observed with NIRSpec, leading to 25 robust redshift measurements. We measure a low fraction of lower-z interlopers, with only two objects (8%) identified as such. Such a high confirmation rate at $z > 8$ reinforces the surprisingly high number densities and brightness of early galaxies compared to the theoretical predictions found by many photometric works in the literature.

Galaxy selection from deep JWST/NIRCam imaging is essential to minimize selection bias at the highest redshifts. The JWST/NIRSpec prism is an optimal tool for measuring such high redshifts, but observations deeper than those of CEERS will be necessary to achieve a higher degree of spectroscopic completeness.

Acknowlegments

We thank the Space Telescope Science Institute (STScI) and GTO NIRSpec teams for their invaluable efforts to make the best out of such a wonderful spectrograph. In particular, we especially thank James Muzerolle, Alaina Henry, Patrick Ogle, Pierre Ferruit, Peter Jakobsen, Diane Karakla, Maria Peña-Guerrero, Amaya Moro-Martín, and James Davies for their frequent assistance with the development of the CEERS NIRSpec observations. We also thank Rychard Bouwens, Callum Donnan, and Ryan Endsley for providing updated samples of their early high-z selections, and the anonymous referee for a very fast and positive review.

This work is based on observations with the NASA/ESA/CSA James Webb Space Telescope obtained from the Mikulski Archive for Space Telescopes at the STScI, which is operated by the Association of Universities for Research in Astronomy (AURA), Incorporated, under NASA contract NAS5-03127. The specific observations analyzed can be accessed via doi: 10.17909/z7p0-8481.

We acknowledge support from NASA through STScI ERS award JWST-ERS-1345.

Software: Astropy (Astropy Collaboration et al. 2022); Bagpipes (Carnall et al. 2018); Cigale (Burgarella et al. 2005; Noll et al. 2009; Boquien et al. 2019); Dense Basis (Iyer et al. 2019); emcee (Foreman-Mackey et al. 2013); Galfit (Peng et al. 2002, 2010); LiMe (Fernández et al. 2023); Mosviz (Developers et al. 2023); and Source Extractor (Bertin & Arnouts 1996).

Appendix A
Complete Census of $z > 8$ Spectroscopic Follow Up in the CEERS Field

Here we present a compilation of all photometric $z > 8$ candidates in CEERS with spectroscopic follow up in either the CEERS observations or the public DD #2750 program. Table 6 presents all objects with robust spectroscopic measurements, while targets undetected or with uncertain spectroscopic measurements are shown in Table 7.

Table 6
Complete Sample of CEERS $z > 8$ Candidates with Robust Spectroscopic Measurements

Source ID	MSA ID	R.A. (deg)	Decl. (deg)	$M_{\rm UV}$ (AB)	$m_{\rm F277W}$ (AB)	Photo. Ref.	$z_{\rm phot}$	$z_{\rm spec}$	Spec. References
(1)	(2)	(3)	(4)	(5)	(6)	(7)	(8)	(9)	(10)
CEERS_16943	D1	214.943152	52.942442	$-20.1^{+0.1}_{-0.1}$	27.9	B23	$11.60^{+0.40}_{-0.50}$	$11.416^{+0.005}_{-0.005}$	AH23
						D23	$12.29^{+0.91}_{-0.32}$		
						F23	$11.08^{+0.39}_{-0.36}$		
						H23b	$11.63^{+0.51}_{-0.53}$		
CEERS_11384	D10	214.906640	52.945504	$-20.3^{+0.1}_{-0.2}$	27.3	D23	$11.27^{+0.58}_{-0.27}$	$11.043^{+0.003}_{-0.003}$	AH23,H23a
						F23	$11.02^{+0.39}_{-0.27}$		
CEERS_19996	D64	214.922787	52.911529	$-19.3^{+0.2}_{-0.2}$	28.3	D23	$11.27^{+0.39}_{-0.70}$	$10.10^{+0.13}_{-0.26}$	AH23
						F23	$11.32^{+0.30}_{-0.90}$		
CEERS_35590	80041	214.732525	52.758090	$-20.1^{+0.1}_{-0.1}$	27.7	F23	$10.15^{+0.36}_{-0.42}$	$10.01^{+0.14}_{-0.19}$	This work
CEERS_99715	80026	214.811852	52.737110	$-20.5^{+0.1}_{-0.1}$	27.1	F23	$9.76^{+0.60}_{-0.09}$	$9.77^{+0.37}_{-0.29}$	This work
CEERS_61419	24	214.897232	52.843854	$-19.3^{+0.2}_{-0.1}$	28.1	B23	$10.20^{+0.60}_{-0.70}$	$8.998^{+0.001}_{-0.001}$	Fu23,T23
						D23	$10.56^{+0.25}_{-0.52}$		
						F23	$8.95^{+1.65}_{-0.06}$		
						W23	$8.95^{+0.07}_{-0.09}$		
CEERS_61381	23	214.901252	52.846997	$-18.9^{+0.2}_{-0.1}$	28.5	D23	$10.45^{+0.52}_{-0.96}$	$8.881^{+0.001}_{-0.001}$	Fu23,T23
						F23	$11.29^{+0.21}_{-1.56}$		
CEERS_7078	7	215.011708	52.988303	$-20.6^{+0.1}_{-0.1}$	27.1	F23	$8.98^{+0.06}_{-0.06}$	$8.876^{+0.002}_{-0.002}$	Fu23,N23
						W23	$9.00^{+0.05}_{-0.06}$		
CEERS_4702	2	214.994404	52.989378	$-20.2^{+0.1}_{-0.1}$	27.5	B23	$9.20^{+0.10}_{-0.20}$	$8.809^{+0.003}_{-0.003}$	Fu23
						F23	$8.98^{+0.12}_{-0.12}$		
						W23	$8.92^{+0.09}_{-0.09}$		
CEERS_43833	D28	214.938642	52.911749	$-20.7^{+0.1}_{-0.1}$	26.8	F23	$9.01^{+0.09}_{-0.09}$	$8.763^{+0.001}_{-0.001}$	AH23
CEERS_43725	1025	214.967532	52.932953	$-21.3^{+0.1}_{-0.1}$	26.3	F23	$8.68^{+0.06}_{-0.09}$	$8.715^{+0.001}_{-0.001}$	He23,T23
CEERS_81061	1019	215.035392	52.890667	$-22.2^{+0.1}_{-0.1}$	25.0	F23	$8.68^{+0.06}_{-0.03}$	$8.679^{+0.001}_{-0.001}$	He23,I23,La23 S23,T23,Z15
CEERS_90671	80083	214.961276	52.842364	$-18.7^{+0.1}_{-0.1}$	28.1	F23	$8.68^{+0.21}_{-0.27}$	$8.638^{+0.001}_{-0.001}$	This work
EGS_11855	1029	215.218762	53.069862	—	—	F23	$8.95^{+0.15}_{-0.43}$	$8.610^{+0.001}_{-0.001}$	He23,T23
EGS_34697	1149	215.089714	52.966183	—	—	F23	$6.45^{+0.68}_{-4.82}$	$8.175^{+0.001}_{-0.001}$	He23,S23,T23
CEERS_4774	3	215.005185	52.996577	$-19.6^{+0.3}_{-0.3}$	27.0	F23	$8.92^{+1.35}_{-0.66}$	$8.005^{+0.001}_{-0.001}$	Fu23,N23,T23
CEERS_4777	4	215.005365	52.996697	$-18.7^{+0.5}_{-0.2}$	28.0	B23	$9.90^{+0.80}_{-0.80}$	$7.993^{+0.001}_{-0.001}$	Fu23
						F23	$10.12^{+0.93}_{-0.69}$		
						L23	$8.62^{+0.34}_{-0.57}$		
CEERS_19185	D355	214.944766	52.931450	$-19.0^{+0.1}_{-0.1}$	28.7	F23	$8.20^{+0.33}_{-0.24}$	$7.925^{+0.001}_{-0.001}$	AH23
CEERS_59920	1027	214.882994	52.840416	$-20.8^{+0.1}_{-0.1}$	26.5	E22	$7.82^{+0.04}_{-0.03}$	$7.820^{+0.001}_{-0.001}$	He23,S23,T23
						F23	$8.17^{+0.06}_{-0.12}$		
EGS_8901	1023	215.188413	53.033647	—	—	F23	$8.85^{+0.18}_{-1.15}$	$7.776^{+0.001}_{-0.001}$	He23,T23
CEERS_23084	20	214.830685	52.887771	$-17.6^{+0.1}_{-0.6}$	28.2	F23	$8.77^{+0.45}_{-0.69}$	$7.769^{+0.003}_{-0.003}$	Fu23
						L23	$9.08^{+0.31}_{-0.38}$		

Table 6
(Continued)

Source ID	MSA ID	R.A. (deg)	Decl. (deg)	M_{UV} (AB)	m_{F277W} (AB)	Photo. Ref.	z_{phot}	z_{spec}	Spec. References
(1)	(2)	(3)	(4)	(5)	(6)	(7)	(8)	(9)	(10)
EGS_33634	686	215.150862	52.989562	—	—	F23	$8.00^{+0.52}_{-1.03}$	$7.752^{+0.001}_{-0.001}$	J22,J23,T23
CEERS_96937	80025	214.806065	52.750867	$-20.0^{+0.2}_{-0.1}$	27.4	F23	$8.47^{+0.15}_{-0.24}$	$7.651^{+0.002}_{-0.001}$	This work
EGS_36986	689	214.999053	52.941977	—	—	F23	$8.61^{+0.11}_{-1.45}$	$7.546^{+0.001}_{-0.001}$	J22,J23,T23
CEERS_24015	746	214.809155	52.868481	$-14.1^{+1.1}_{-0.7}$	28.1	L23	$8.14^{+0.45}_{-1.71}$	$5.623^{+0.001}_{-0.001}$	K23
CEERS_13256	D0	214.914550	52.943023	$-16.2^{+0.5}_{-0.1}$	26.5	B23	$16.30^{+0.30}_{-0.40}$	$4.912^{+0.001}_{-0.001}$	AH23
						D23	$16.39^{+0.32}_{-0.22}$		
						F23	$16.45^{+0.18}_{-0.45}$		
						H23b	$16.25^{+0.24}_{-0.46}$		

Note. (1) Source ID in the CEERS catalog. Galaxies out of the CEERS NIRCam imaging footprint are identified with their CANDELS EGS ID from Stefanon et al. (2017). (2) ID in the MSA observations. Those preceded by a letter "D" correspond to observations from the DD #2750 program. (3) R.A.(J2000). (4) Decl.(J2000). (5) Absolute UV magnitude measured at rest-frame 1500 Å. (6) Apparent magnitude in the NIRCam/F277W band. (7) Reference for the photometric redshift: B23 (Bouwens et al. 2023); D23 (Donnan et al. 2023); E22 (Endsley et al. 2022); H23b (Harikane et al. 2023b); L23 (Labbé et al. 2023); and W23 (Whitler et al. 2023). Objects labeled as F23 include both sources from Finkelstein et al. (2023) and new sources in the complete CEERS NIRCam coverage selected following the same criteria used in that work. (8) Photometric redshift. (9) Spectroscopic redshift remeasured in this work for emission lines redshifts following the methodology described in Section 3.1. (10) Works spectroscopically reporting these sources: AH23 (Arrabal Haro et al. 2023); Fu23 (Fujimoto et al. 2023); He23 (Heintz et al. 2023); I23 (Isobe et al. 2023); J22 (Jung et al. 2022); J23 (Jung et al. 2023); K23 (Kocevski et al. 2023); La23 (Larson et al. 2023); N23 (Nakajima et al. 2023); S23 (Sanders et al. 2023); T23 (Tang et al. 2023); and Z15 (Zitrin et al. 2015).

Table 7
Complete Sample of CEERS $z > 8$ Candidates in NIRSpec MSA Observations without Robust Spectroscopic Redshift. See the Column Descriptions in Table 6

Source ID	MSA ID	R.A. (deg)	Decl. (deg)	m_{F277W} (AB)	Photo. References	z_{phot}
(1)	(2)	(3)	(4)	(5)	(6)	(7)
CEERS_2067	0	215.010022	53.013641	27.8	F23	$13.69^{+0.66}_{-0.99}$
CEERS_49703	733	214.910343	52.855032	28.4	D23	$11.90^{+0.70}_{-1.60}$
CEERS_87379	80073	214.932064	52.841873	27.3	F23	$11.08^{+0.24}_{-0.48}$
CEERS_10332	9	215.043999	52.994302	28.4	D23	$10.80^{+0.51}_{-0.40}$
					F23	$10.57^{+0.18}_{-1.05}$
CEERS_57400	22	214.869661	52.843646	28.7	F23	$10.60^{+0.60}_{-0.66}$
CEERS_13452	D69	214.861602	52.904604	28.2	D23	$10.56^{+1.10}_{-0.30}$
					F23	$9.55^{+0.78}_{-0.09}$
CEERS_36952	80099	214.771106	52.780817	29.1	F23	$10.48^{+6.00}_{-0.81}$
CEERS_42447	80042	214.795552	52.767286	28.3	F23	$10.30^{+0.09}_{-1.11}$
CEERS_4821	853	215.012542	53.001372	27.5	W23	$9.16^{+0.06}_{-0.06}$
CEERS_56878	21	214.888127	52.858987	27.7	F23	$9.01^{+0.30}_{-0.30}$

Appendix B
Measuring and Rescaling Noise in the NIRSpec Spectra

The JWST pipeline resamples the 2D NIRSpec MSA spectra in order to align and combine the individual nodded exposures and to rectify the 2D spectra so that the dispersion and cross-dispersion axes align with the x and y pixel coordinates in the `s2d` pipeline data product. The pipeline then extracts a 1D spectrum (`x1d`) from the `s2d` product, including `FLUX` and `FLUX_ERROR` values. The flux errors are calculated by the pipeline using an instrumental noise model, and the resampling introduces correlation between pixels that smooth the data, reducing the rms of the measured pixel values.

We test the flux errors in the `x1d` spectra for our faint galaxy targets CEERS_99715 and CEERS_35590 by dividing the fluxes by the flux errors to calculate an S/N spectrum. These galaxies are very faint, without strong emission lines or other features so that `FLUX_ERROR` should be dominated by background and instrument noise. After masking pixel artifacts

and missing data (Section 2.4) we smooth the S/N spectrum by a 30 pixel boxcar filter and subtract to produce a residual noise spectrum with zero mean and approximately constant dispersion over the full wavelength range. If the noise in the data has a Gaussian distribution and is correctly characterized by the pipeline's FLUX_ERROR values, the values of this residual noise spectrum should be Gaussian with $\sigma = 1$. The noise residuals for both objects show nearly Gaussian distributions with $\sigma_{S/N} = 1.30$ and 1.24 for objects CEERS_99715 and CEERS_35590, respectively.

We also measure the autocorrelation function $\xi(\delta x)$ of the S/N spectrum as a function of pixel lag δx. For uncorrelated random noise, ξ would be a delta function at $\delta x = 0$. Instead, we observe positive correlation on a scale of $|\delta x| = 1$ to 2 pixels. The 30 pixel boxcar subtraction also introduces anticorrelation out to scales of $|\delta x| = 3$ to 15 pixels. We calculate the excess correlation over this negative "background" measured at $|\delta x| = 3$ pixels:

$$X = \sum_{\delta x=-2}^{+2} (\xi(\delta x) - \xi(|\delta x| = 3)).$$

For noise with intrinsic rms $= \sigma_0$, interpolation reduces the apparent rms $= \sigma_{obs}$ by a factor F:

$$\sigma_{obs} = \sigma_0 / F,$$
$$F = \sqrt{X/\xi(0)}.$$

We measure $F = 1.42$ and 1.33 for objects CEERS_99715 and CEERS_35590, respectively. Multiplying F by the rms rescaling factors $\sigma_{S/N}$ calculated above, we derive total error correction factors of 1.85 and 1.65 for these two objects, respectively, and multiply the pipeline FLUX_ERROR values by these factors. We expect the noise scaling and correlation to be similar for the prism spectra of all faint galaxy targets, and therefore adopt a noise rescaling factor of 1.75 for the other objects analyzed in this paper.

Appendix C
Caveat on the Robustness of the Photometric Selection: Possible Interlopers in Relaxed Photometric Samples

We note here that the primary photometric sample of seven $z > 8$ galaxies was selected via a robust set of photometric detection and photometric-redshift-based selection criteria. As fully described in Finkelstein et al. (2023), our photometric redshift selection makes use of several integrals of the photometric redshift $P(z)$, rather than relying solely on the best-fitting redshift.

Figure 9 shows the 1D and 2D spectra of one of these objects, CEERS_87103 (MSA ID 80072), observed in CEERS epoch 3. The spectra reveal an unambiguous redshift of $z = 5.27$ based on the Hα and [O III] emission lines. The right-hand panel shows its $P(z)$ peaking at $z \sim 8$, which led to our placing of a slit on it. However, this distribution is also quite broad, with several peaks at lower redshift. This galaxy was labeled as a less-secure high-z candidate for two specific reasons. First, the integral of $P(z)$ at $z > 7$ was 0.55, less than the threshold of 0.7 adopted by Finkelstein et al. (2023). Second, the difference in the goodness-of-fit χ^2 value between the primary $z \sim 8$ peak and the highest lower-redshift, $z \sim 5$, peak was 1.5, much less than the threshold of 4 adopted by Finkelstein et al. (2023). This highlights the importance of employing robust selection criteria in defining high-z samples, as more relaxed high-z selections based solely on the best-fitting redshift can be prone to include lower-z interlopers in the selected samples.

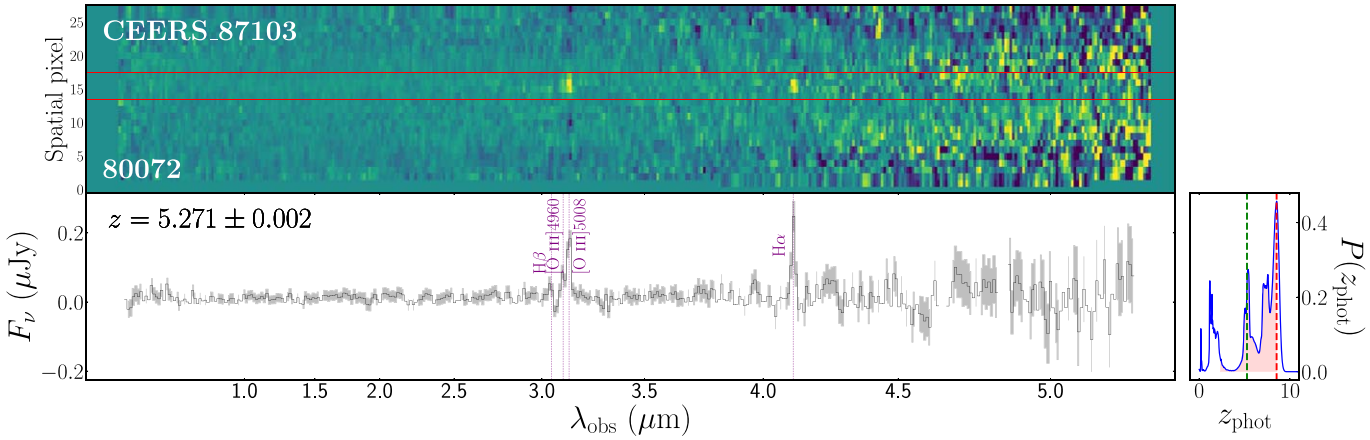

Figure 9. 1D (bottom left) and 2D (top left) spectra of CEERS_87103. The two red horizontal lines in the 2D spectrum show the spatial window employed to extract the 1D spectrum, and the flux uncertainties of the 1D spectrum are represented by the shaded gray regions. The broad photometric redshift probability distribution function $P(z)$ obtained for this source (right) peaks at $z = 8.53$ (dashed red line), which could result in the inclusion of an object like this in high-z samples under relaxed selection criteria. The shaded red region behind the $P(z)$ shows the 68% confidence interval of the photometric redshift estimation, with the dashed green line indicating the spectroscopic value.

ORCID iDs

Pablo Arrabal Haro https://orcid.org/0000-0002-7959-8783
Mark Dickinson https://orcid.org/0000-0001-5414-5131
Steven L. Finkelstein https://orcid.org/0000-0001-8519-1130
Seiji Fujimoto https://orcid.org/0000-0001-7201-5066
Vital Fernández https://orcid.org/0000-0003-0531-5450
Jeyhan S. Kartaltepe https://orcid.org/0000-0001-9187-3605
Intae Jung https://orcid.org/0000-0003-1187-4240
Justin W. Cole https://orcid.org/0000-0002-6348-1900
Denis Burgarella https://orcid.org/0000-0002-4193-2539
Katherine Chworowsky https://orcid.org/0000-0003-4922-0613
Taylor A. Hutchison https://orcid.org/0000-0001-6251-4988
Alexa M. Morales https://orcid.org/0000-0003-4965-0402
Casey Papovich https://orcid.org/0000-0001-7503-8482
Raymond C. Simons https://orcid.org/0000-0002-6386-7299
Ricardo O. Amorín https://orcid.org/0000-0001-5758-1000
Bren E. Backhaus https://orcid.org/0000-0001-8534-7502
Micaela B. Bagley https://orcid.org/0000-0002-9921-9218
Laura Bisigello https://orcid.org/0000-0003-0492-4924
Antonello Calabrò https://orcid.org/0000-0003-2536-1614
Marco Castellano https://orcid.org/0000-0001-9875-8263
Nikko J. Cleri https://orcid.org/0000-0001-7151-009X
Romeel Davé https://orcid.org/0000-0003-2842-9434
Avishai Dekel https://orcid.org/0000-0003-4174-0374
Henry C. Ferguson https://orcid.org/0000-0001-7113-2738
Adriano Fontana https://orcid.org/0000-0003-3820-2823
Eric Gawiser https://orcid.org/0000-0003-1530-8713
Mauro Giavalisco https://orcid.org/0000-0002-7831-8751
Santosh Harish https://orcid.org/0000-0003-0129-2079
Nimish P. Hathi https://orcid.org/0000-0001-6145-5090
Michaela Hirschmann https://orcid.org/0000-0002-3301-3321
Benne W. Holwerda https://orcid.org/0000-0002-4884-6756
Marc Huertas-Company https://orcid.org/0000-0002-1416-8483
Anton M. Koekemoer https://orcid.org/0000-0002-6610-2048
Rebecca L. Larson https://orcid.org/0000-0003-2366-8858
Ray A. Lucas https://orcid.org/0000-0003-1581-7825
Bahram Mobasher https://orcid.org/0000-0001-5846-4404
Pablo G. Pérez-González https://orcid.org/0000-0003-4528-5639
Nor Pirzkal https://orcid.org/0000-0003-3382-5941
Caitlin Rose https://orcid.org/0000-0002-8018-3219
Paola Santini https://orcid.org/0000-0002-9334-8705
Jonathan R. Trump https://orcid.org/0000-0002-1410-0470
Alexander de la Vega https://orcid.org/0000-0002-6219-5558
Xin Wang https://orcid.org/0000-0002-9373-3865
Benjamin J. Weiner https://orcid.org/0000-0001-6065-7483
Stephen M. Wilkins https://orcid.org/0000-0003-3903-6935
Guang Yang https://orcid.org/0000-0001-8835-7722
L. Y. Aaron Yung https://orcid.org/0000-0003-3466-035X
Jorge A. Zavala https://orcid.org/0000-0002-7051-1100

References

Adams, N. J., Conselice, C. J., Ferreira, L., et al. 2023, MNRAS, 518, 4755
Arrabal Haro, P., Dickinson, M., Finkelstein, S. L., et al. 2023, arXiv:2303.15431
Arrabal Haro, P., Rodríguez Espinosa, J. M., Muñoz-Tuñón, C., et al. 2018, MNRAS, 478, 3740
Astropy Collaboration, Price-Whelan, A. M., Lim, P. L., et al. 2022, ApJ, 935, 167
Atek, H., Shuntov, M., Furtak, L. J., et al. 2023, MNRAS, 519, 1201
Austin, D., Adams, N. J., Conselice, C. J., et al. 2023, arXiv:2302.04270
Bagley, M. B., Finkelstein, S. L., Koekemoer, A. M., et al. 2023, ApJL, 946, L12
Beichman, C. A., Rieke, M., Eisenstein, D., et al. 2012, Proc. SPIE, 8442, 84422N
Bertin, E., & Arnouts, S. 1996, A&AS, 117, 393
Boquien, M., Burgarella, D., Roehlly, Y., et al. 2019, A&A, 622, A103
Bouwens, R., Illingworth, G., Oesch, P., et al. 2023, MNRAS, 523, 1009
Bouwens, R. J., Illingworth, G. D., Oesch, P. A., et al. 2015, ApJ, 803, 34
Bowler, R. A. A., Jarvis, M. J., Dunlop, J. S., et al. 2020, MNRAS, 493, 2059
Boyett, K., Trenti, M., Leethochawalit, N., et al. 2023, arXiv:2303.00306
Boylan-Kolchin, M. 2023, NatAs, 7, 731
Brammer, G. B., van Dokkum, P. G., & Coppi, P. 2008, ApJ, 686, 1503
Bunker, A. J., Saxena, A., Cameron, A. J., et al. 2023, arXiv:2302.07256
Burgarella, D., Buat, V., & Iglesias-Páramo, J. 2005, MNRAS, 360, 1413
Calzetti, D., Armus, L., Bohlin, R. C., et al. 2000, ApJ, 533, 682
Calzetti, D., Kinney, A. L., & Storchi-Bergmann, T. 1994, ApJ, 429, 582
Carnall, A. C., Leja, J., Johnson, B. D., et al. 2019a, ApJ, 873, 44
Carnall, A. C., McLure, R. J., Dunlop, J. S., et al. 2019b, MNRAS, 490, 417
Carnall, A. C., McLure, R. J., Dunlop, J. S., & Davé, R. 2018, MNRAS, 480, 4379
Castellano, M., Fontana, A., Treu, T., et al. 2022, ApJL, 938, L15
Chabrier, G. 2003, PASP, 115, 763
Curtis-Lake, E., Carniani, S., Cameron, A., et al. 2023, NatAs, 7, 622
Davé, R., Anglés-Alcázar, D., Narayanan, D., et al. 2019, MNRAS, 486, 2827
Dekel, A., Sarkar, K. C., Birnboim, Y., Mandelker, N., & Li, Z. 2023, MNRAS, 523, 3201
Developers, J., Averbukh, J., Bradley, L., et al. 2023, Jdaviz, Zenodo, doi: 10.5281/zenodo.7504710
Dijkstra, M. 2014, PASA, 31, e040
Donnan, C. T., McLeod, D. J., Dunlop, J. S., et al. 2023, MNRAS, 518, 6011
Eldridge, J. J., Stanway, E. R., Xiao, L., et al. 2017, PASA, 34, e058
Ellis, R. S., McLure, R. J., Dunlop, J. S., et al. 2013, ApJL, 763, L7
Endsley, R., Stark, D. P., Whitler, L., et al. 2022, arXiv:2208.14999
Fernández, V., Amorín, R., Sanchez-Janssen, R., del Valle-Espinosa, M. G., & Papaderos, P. 2023, MNRAS, 520, 3576
Ferrara, A., Pallottini, A., & Dayal, P. 2023, MNRAS, 522, 3986
Ferruit, P., Jakobsen, P., Giardino, G., et al. 2022, A&A, 661, A81
Finkelstein, S. L., & Bagley, M. B. 2022, ApJ, 938, 25
Finkelstein, S. L., Bagley, M. B., Arrabal Haro, P., et al. 2022, ApJL, 940, L55
Finkelstein, S. L., Bagley, M. B., Ferguson, H. C., et al. 2023, ApJL, 946, L13
Finkelstein, S. L., D'Aloisio, A., Paardekooper, J.-P., et al. 2019, ApJ, 879, 36
Finkelstein, S. L., Ryan, R. E. J., Papovich, C., et al. 2015, ApJ, 810, 71
Foreman-Mackey, D., Hogg, D. W., Lang, D., & Goodman, J. 2013, PASP, 125, 306
Fujimoto, S., Arrabal Haro, P., Dickinson, M., et al. 2023, ApJL, 949, L25
Giavalisco, M. 2002, ARA&A, 40, 579
Grogin, N. A., Kocevski, D. D., Faber, S. M., et al. 2011, ApJS, 197, 35
Harikane, Y., Nakajima, K., Ouchi, M., et al. 2023a, arXiv:2304.06658
Harikane, Y., Ouchi, M., Oguri, M., et al. 2023b, ApJS, 265, 5
Hastings, W. K. 1970, Biometrika, 57, 97
Hayes, M. 2015, PASA, 32, e027
Heintz, K. E., Brammer, G. B., Giménez-Arteaga, C., et al. 2023, arXiv:2212.02890
Hsiao, T. Y.-Y., Abdurro'uf, C. D., Coe, D., et al. 2023, arXiv:2305.03042
Isobe, Y., Ouchi, M., Nakajima, K., et al. 2023, arXiv:2301.06811
Iyer, K. G., Gawiser, E., Faber, S. M., et al. 2019, ApJ, 879, 116
Jakobsen, P., Ferruit, P., Alves de Oliveira, C., et al. 2022, A&A, 661, A80
Jiang, L., Kashikawa, N., Wang, S., et al. 2021, NatAs, 5, 256
Jung, I., Finkelstein, S. L., Arrabal Haro, P., et al. 2023, arXiv:2304.05385
Jung, I., Finkelstein, S. L., Larson, R. L., et al. 2022, arXiv:2212.09850
Jung, I., Finkelstein, S. L., Song, M., et al. 2017, ApJ, 834, 81
Kocevski, D. D., Onoue, M., Inayoshi, K., et al. 2023, arXiv:2302.00012
Koekemoer, A. M., Faber, S. M., Ferguson, H. C., et al. 2011, ApJS, 197, 36
Labbé, I., van Dokkum, P., Nelson, E., et al. 2023, Natur, 616, 266

Larson, R. L., Finkelstein, S. L., Kocevski, D. D., et al. 2023, arXiv:2303.08918
Larson, R. L., Hutchison, T. A., Bagley, M., et al. 2022, arXiv:2211.10035
Leja, J., Carnall, A. C., Johnson, B. D., Conroy, C., & Speagle, J. S. 2019, ApJ, 876, 3
Mascia, S., Pentericci, L., Calabrò, A., et al. 2023, A&A, 672, A155
Mason, C. A., Trenti, M., & Treu, T. 2023, MNRAS, 521, 497
Matthee, J., Mackenzie, R., Simcoe, R. A., et al. 2023, ApJ, 950, 67
Matthee, J. J. A., Sobral, D., Swinbank, A. M., et al. 2014, MNRAS, 440, 2375
McLure, R. J., Dunlop, J. S., Bowler, R. A. A., et al. 2013, MNRAS, 432, 2696
Metropolis, N., Rosenbluth, A. W., Rosenbluth, M. N., Teller, A. H., & Teller, E. 1953, JChPh, 21, 1087
Naidu, R. P., Oesch, P. A., Setton, D. J., et al. 2022a, arXiv:2208.02794
Naidu, R. P., Oesch, P. A., van Dokkum, P., et al. 2022b, ApJL, 940, L14
Nakajima, K., Ouchi, M., Isobe, Y., et al. 2023, arXiv:2301.12825
Noll, S., Burgarella, D., Giovannoli, E., et al. 2009, A&A, 507, 1793
Oesch, P. A., Bouwens, R. J., Illingworth, G. D., Labbé, I., & Stefanon, M. 2018, ApJ, 855, 105
Oesch, P. A., Brammer, G., van Dokkum, P. G., et al. 2016, ApJ, 819, 129
Oke, J. B., & Gunn, J. E. 1983, ApJ, 266, 713
Osterbrock, D. E. 1989, Astrophysics of Gaseous Nebulae and Active Galactic Nuclei (USA: Univ Science Books)
Pacifici, C., Iyer, K. G., Mobasher, B., et al. 2023, ApJ, 944, 141
Papovich, C., Cole, J., Yang, G., et al. 2023, ApJL, 949, L18
Pei, Y. C. 1992, ApJ, 395, 130
Peng, C. Y., Ho, L. C., Impey, C. D., & Rix, H.-W. 2002, AJ, 124, 266
Peng, C. Y., Ho, L. C., Impey, C. D., & Rix, H.-W. 2010, AJ, 139, 2097
Pérez-González, P. G., Barro, G., Annunziatella, M., et al. 2023a, ApJL, 946, L16
Pérez-González, P. G., Costantin, L., Langeroodi, D., et al. 2023b, arXiv:2302.02429
Planck Collaboration, Aghanim, N., Akrami, Y., et al. 2020, A&A, 641, A6
Rieke, M. J., Baum, S. A., Beichman, C. A., et al. 2003, Proc. SPIE, 4850, 478
Rieke, M. J., Kelly, D., & Horner, S. 2005, Proc. SPIE, 5904, 1
Roberts-Borsani, G., Treu, T., Chen, W., et al. 2023, Natur, 618, 480
Robertson, B. E., Tacchella, S., Johnson, B. D., et al. 2023, NatAs, 7, 611
Rodighiero, G., Bisigello, L., Iani, E., et al. 2023, MNRAS, 518, L19
Sanders, R. L., Shapley, A. E., Topping, M. W., Reddy, N. A., & Brammer, G. B. 2023, arXiv:2303.08149
Sobral, D., Santos, S., Matthee, J., et al. 2018, MNRAS, 476, 4725
Somerville, R. S., Olsen, C., Yung, L. Y. A., et al. 2021, MNRAS, 502, 4858
Somerville, R. S., Popping, G., & Trager, S. C. 2015, MNRAS, 453, 4337
Stefanon, M., Labbé, I., Bouwens, R. J., et al. 2019, ApJ, 883, 99
Stefanon, M., Yan, H., Mobasher, B., et al. 2017, ApJS, 229, 32
Storey, P. J., & Zeippen, C. J. 2000, MNRAS, 312, 813
Tacchella, S., Eisenstein, D. J., Hainline, K., et al. 2023, arXiv:2302.07234
Tang, M., Stark, D. P., Chen, Z., et al. 2023, arXiv:2301.07072
Treu, T., Calabrò, A., Castellano, M., et al. 2023, ApJL, 942, L28
Treu, T., Roberts-Borsani, G., Bradac, M., et al. 2022, ApJ, 935, 110
Trump, J. R., Arrabal Haro, P., Simons, R. C., et al. 2023, ApJ, 945, 35
Whitler, L., Endsley, R., Stark, D. P., et al. 2023, MNRAS, 519, 157
Williams, H., Kelly, P. L., Chen, W., et al. 2023, Sci, 380, 416
Yan, H., Ma, Z., Ling, C., Cheng, C., & Huang, J.-S. 2023, ApJL, 942, L9
Yang, G., Caputi, K. I., Papovich, C., et al. 2023, ApJL, 950, L5
Yung, L. Y. A., Somerville, R. S., Finkelstein, S. L., Popping, G., & Davé, R. 2019a, MNRAS, 483, 2983
Yung, L. Y. A., Somerville, R. S., Popping, G., et al. 2019b, MNRAS, 490, 2855
Yung, L. Y. A., Somerville, R. S., Finkelstein, S. L., Wilkins, S. M., & Gardner, J. P. 2023, arXiv:2304.04348
Zavala, J. A., Buat, V., Casey, C. M., et al. 2023, ApJL, 943, L9
Zitrin, A., Labbé, I., Belli, S., et al. 2015, ApJL, 810, L12